Eur. J. Mineral., 36, 879–898, 2024
https://doi.org/10.5194/ejm-36-879-2024

European Journal of Mineralogy
Open Access

Multifaceted orogenic fluid dynamics unraveled by hydrothermal epidote

Veronica Peverelli[1], Alfons Berger[1], Martin Wille[1], Thomas Pettke[1], Benita Putlitz[2], Andreas Mulch[3,4], Edwin Gnos[5], and Marco Herwegh[1]

[1]Department of Geological Sciences, University of Bern, 3012 Bern, Switzerland
[2]Institute of Earth Sciences, University of Lausanne, 1015 Lausanne, Switzerland
[3]Senckenberg Biodiversity and Climate Research Centre (SBiK-F), 60325 Frankfurt, Germany
[4]Institute of Geosciences, Goethe University Frankfurt, 60438 Frankfurt, Germany
[5]Muséum d'histoire naturelle de Genève, 1208 Geneva, Switzerland

Correspondence: Veronica Peverelli (veronica.peverelli@unibe.ch)

Received: 30 May 2024 – Revised: 9 August 2024 – Accepted: 13 August 2024 – Published: 24 September 2024

Abstract. Characterizing fluid circulation in orogens is key to understanding orogenic processes because fluid–rock interaction modifies the physical properties of rocks, hence their response to deformation and, for example, their suitability for radioactive waste storage. Fluid circulation can be dated by applying geochronological methods to fluid-precipitated minerals. Fluid sources and associated pathways can be traced using isotope data measured in the same or in other cogenetic minerals. We applied this concept to the Aar Massif (central Swiss Alps), which was part of the former European passive continental margin that was deformed and exhumed during the (Cenozoic) Alpine orogeny. Newly collected epidote from veins and from one cleft at several localities in meta-granitoids in the Aar Massif yielded U–Pb ages ranging from 27.7 ± 3.4 to 12.4 ± 1.9 Ma, which complement previously published geochronological data revealing Permian (278 ± 29, 251 ± 50, and 275 ± 18 Ma) and Miocene (19.2 ± 4.3 and 16.9 ± 3.7 Ma) epidote veins. We used Pb–Sr–O–H isotope geochemistry of epidote to evaluate fluid sources and pathways during Permian rifting and the Miocene compressional phases of Alpine orogeny. Strontium isotope data of Permian epidote are consistent with previous work suggesting meteoric water infiltration along syn-rift faults and through syn-rift sediments. A more-complex structural framework existed in the Miocene, when a sedimentary lid covered the Aar Massif. Strontium, O, and H isotope data of Miocene epidote-forming fluids indicate (1) meteoric water, mixing with (2) fluids derived from sedimentary units being compacted during orogenesis and/or (3) metamorphic water. All three fluid endmembers may have been circulating and mixing in the Aar Massif during Miocene deformation. Strontium isotope data further indicate that Miocene fluids contributed to imprinting a highly radiogenic Sr isotope composition onto Alpine shear zones or that the fluids inherited a highly radiogenic Sr isotope component by dissolving the Rb-rich, high $^{87}Sr/^{86}Sr$ biotite therein. Both possibilities can coexist, and they imply that external fluids could modify the chemical composition of the post-Variscan granitoids hosting the studied epidote veins by fluid–rock interaction processes during deformation. Lead, Sr, and H isotopic differences among Miocene samples further suggest complexity of large-scale fluid circulation. Our work supports the fact that the reconstruction of multifaceted and multi-stage fluid circulation in highly deformed rocks benefits from extracting geochronological and isotope data from the same mineral.

1 Introduction

Fluid circulation in the granitic continental crust can lead to the formation of ore deposits (e.g., Yardley, 2005; Yardley and Cleverley, 2015; Bodnar et al., 2014), crucial in sustaining modern economies. However, fluid flow can have adverse effects as well, such as hampering the suitability of a lithology as a reservoir for storage of radioactive waste, given the risks posed to the environment and to the population if radioactive elements are redistributed towards the surface or groundwater reservoirs. In addition, fluid–rock interaction processes cause the weakening of granitoids through the substitution of mechanically strong primary magmatic minerals with weak alteration minerals, with far-reaching implications on orogenic processes and strain localization (e.g., Wintsch et al., 1995; Oliot et al., 2010; Goncalves et al., 2012; Malatesta et al., 2021; Wehrens et al., 2016, 2017; Zhan et al., 2024). For these reasons, understanding timing, sources, and pathways of fluid circulation in orogens is relevant for economic, structural, and engineering applications. Key areas have been identified to carry out experiments and surveys leading to a better understanding of fluid circulation dynamics in orogens and in the continental crust therein. One of these is the Grimsel test site (GTS; Fig. 1) of Nagra (the Swiss National Cooperative for the Disposal of Radioactive Waste), which is located in the Aar Massif (central Swiss Alps). In the GTS, multiple experiments have been performed to investigate the suitability of deformed and homogeneous crystalline rocks as reservoirs for storage of radioactive waste (e.g., Keusen et al., 1989; Schneeberger et al., 2019). The GTS is ideal in this respect because the Aar Massif is a typical mid-crustal section with deformation features that can be traced from one end of the massif to the other (Herwegh et al., 2020, 2022). In addition, there is evidence for three main events (Permian, tentatively Triassic, and Miocene/Pliocene) of fluid circulation from the Permian until recent times (see below; Dempster, 1986; Abrecht and Schaltegger, 1988; Marquer and Burkhard, 1992; Marquer and Peucat, 1994; Hofmann et al., 2004; Challandes et al., 2008; Rossi and Rolland, 2009; Goncalves et al., 2012; Janots et al., 2012; Berger et al., 2013, 2017a; Wehrens et al., 2016, 2017; Bergemann et al., 2017; Ricchi et al., 2019; Gnos et al., 2021; Peverelli et al., 2021, 2022a). Although these studies largely demonstrate the occurrence of multistage fluid circulation in the Aar Massif, fluid sources and pathways can be further explored by combining multiple isotope tools.

In this study, we applied U–Pb geochronology and Pb–Sr–O–H isotope geochemistry of epidote (intended here as minerals of the epidote–clinozoisite solid solution) in Permian and Miocene hydrothermal veins collected at several localities in post-Variscan granitoids in the Aar Massif. In addition to ascertaining fluid circulation throughout the exhuming Aar Massif, we discuss fluid sources and pathways of the epidote-forming fluids using, O, H, Pb, and Sr isotope geochemistry. Finally, we address the interplay of syn-orogenic fluids and Miocene shear zones in determining the Sr isotope composition of hydrothermal epidote.

2 Geological setting

The Aar Massif (Fig. 1) is one of the external crystalline massifs of the Alps, forming part of the basement of the former European continental margin (e.g., Schaltegger, 1993; Berger et al., 2017b; Herwegh et al., 2022). Epidote veins occur in the Central Aar Granite, Grimsel Granodiorite and Gastern Granite, which intruded into a polymetamorphic basement in post-Variscan times (297 ± 2, 299 ± 2, and 303 ± 4 Ma, respectively; zircon U–Pb; Schaltegger and Corfu, 1992; Schaltegger, 1993; Ruiz et al., 2022). The Central Aar Granite and Grimsel Granodiorite (described in detail in Schaltegger, 1990; Schaltegger and Corfu, 1992; Schaltegger, 1993; Wehrens et al., 2016, 2017; Schneeberger et al., 2019) are interpreted as having originated from a mantle source, emplaced after Variscan peak metamorphism and compressional deformation (Schaltegger, 1990). The Gastern Granite, on the other hand, is interpreted as a crust-derived granite due to its inheritance of older Pb components (Schaltegger, 1993). During the Alpine orogeny, the southern Aar Massif was deformed at greenschist-facies conditions (450 ± 25 °C and 0.6 ± 0.1 GPa; Goncalves et al., 2012). Alpine deformation produced a large number of shear zones (Steck, 1966; Wehrens et al., 2017; Herwegh et al., 2017, 2020, 2022; Baumberger et al., 2022; Musso Piantelli et al., 2022), and it is subdivided into two main phases: (1) the Handegg phase, characterized by reverse faulting and occurring 25–17 Ma (Challandes et al., 2008; Rolland et al., 2009; Wehrens et al., 2017; Bergemann et al., 2017); (2a) the Oberaar phase in the southern Aar Massif, characterized by dextral strike-slip shearing starting from 14 to 13 Ma (Rolland et al., 2009; Wehrens et al., 2017; Herwegh et al., 2017; 2020), and (2b) the Pfaffenchopf phase in the northern Aar Massif, with northwest-directed thrusting from 13 to 12 Ma (Herwegh et al., 2017; 2020). While a more-detailed description of Alpine shear zones and other regional-scale structures is outside the scope of this work, these are described and depicted in detail in Wehrens et al. (2016, 2017) and Schneeberger et al. (2019).

Multi-stage fluid circulation is recorded in the Aar Massif. The Central Aar Granite and Grimsel Granodiorite were altered by pre-orogenic fluid circulation in two stages: (1) Permian fluid circulation of meteoric origin at 276 ± 13 Ma (averaged from three Permian ages; see Table 1 and Peverelli et al., 2022a) and (2) Triassic or later hydrothermal activity at 234.1 ± 26 Ma and 207.6 ± 26 Ma (Abrecht and Schaltegger, 1988). Extensive fluid circulation is documented during the Alpine orogeny by multiple lines of evidence: crystallization of hydrous phases at the expense of magmatic feldspars in granitoids (e.g., Goncalves et al., 2012) and enrichment

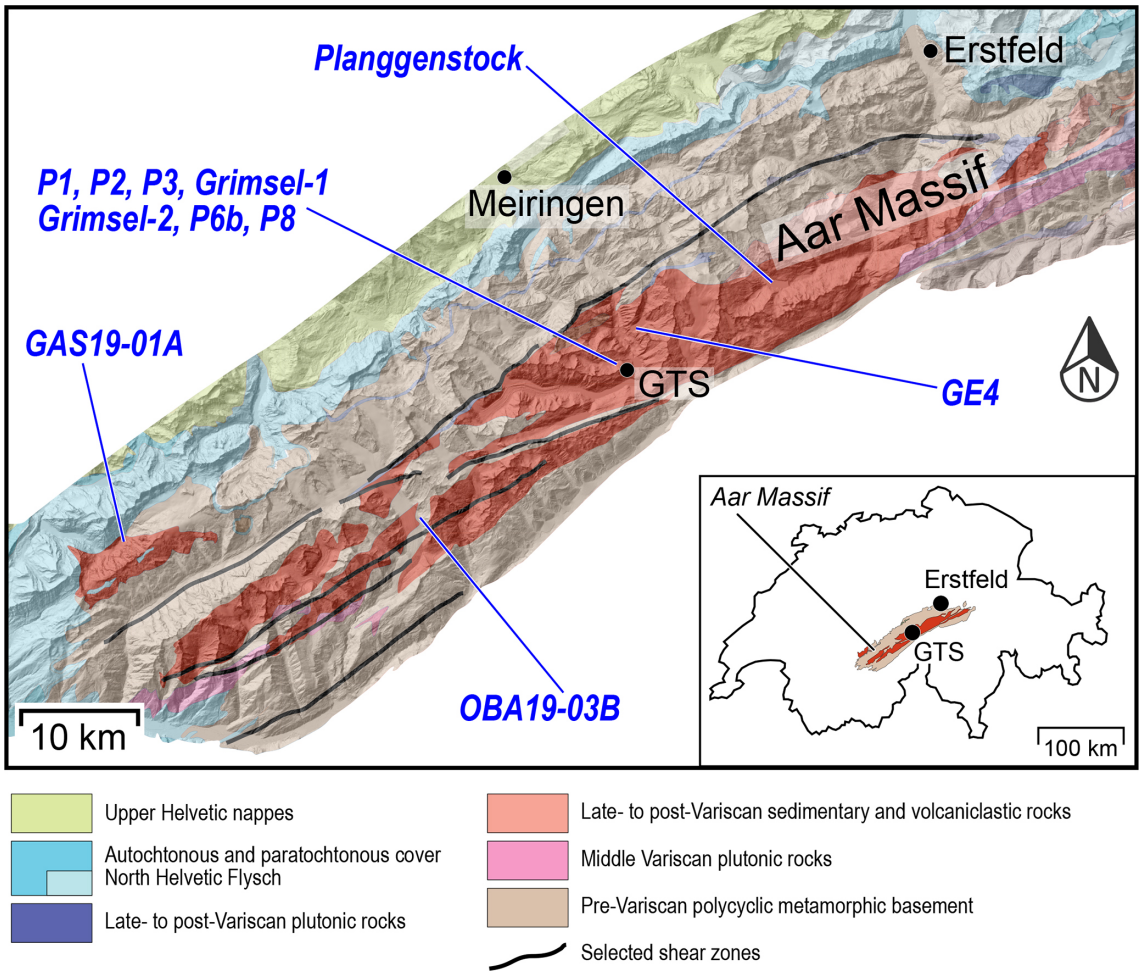

Figure 1. Geological map of the Aar Massif and sampling locations of the epidote samples studied here. The inset shows the location of the Aar Massif in Switzerland. The geological map is redrawn from Berger et al. (2017) and from Musso Piantelli (2023); the inset is redrawn from https://map.geo.admin.ch, last access: 15 May 2024. The digital elevation model is from https://map.geo.admin.ch. GTS is the Grimsel test site.

in hydrothermal minerals in shear zones (e.g., Marquer and Burkhard, 1992; Marquer and Peucat, 1994; Rossi and Rolland, 2009; Wehrens et al., 2016), in veins and clefts (e.g., Janots et al., 2012; Berger et al., 2013; Bergemann et al., 2017; Ricchi et al., 2019; Gnos et al., 2021; Peverelli et al., 2021, 2022a, b), and in hydrothermally mineralized breccias in the Grimsel Pass area, central Aar Massif (where the GTS is located; Fig. 1; Hofmann et al., 2004; Berger and Herwegh, 2019, 2022).

3 Samples

Epidote samples (Fig. 2) were collected throughout the Aar Massif (Fig. 1). Here, we describe and present only those that could be dated successfully (i.e., those with sufficient spread in $^{207}Pb/^{206}Pb$ and $^{238}U/^{206}Pb$ isotopic ratios). It should be noted that unless biotite or chlorite are present in epidote veins (see Challandes et al., 2008; Rolland et al., 2009; Herwegh et al., 2017; Wehrens et al., 2017), vein mineral assemblages alone cannot be related to ages. Minor biotite is detected in only two of the newly studied thin sections (Sect. 3.1). The identification of sub-grain rotation recrystallization is made in comparison with Stipp et al. (2002). All epidote samples are minerals of the epidote–clinozoisite solid solution ($Ca_2Al_2(Al,Fe^{3+})Si_3O_{12}(OH)$; see also Table S4 in the supplementary material). The reader should be aware that new samples are presented in Sect. 3.1 and previously published ones in Sect. 3.2. However, the order in which they are shown in Figs. 2-3 is reversed: previously published samples are in panels (a)-(e) and new samples in panels (f)-(k).

3.1 New samples

Samples P6b and P8 are hosted by the Grimsel granodiorite, and they are associated with a shear zone inside the

https://doi.org/10.5194/ejm-36-879-2024

Table 1. Epidote U–Pb ages, initial Pb and Sr isotope ratios, and O and H isotope data. Age uncertainties are given at 95 % confidence; uncertainties in Pb and Sr isotope ratios are 2 standard errors (2 SE); all oxygen isotope data ($\delta^{18}O$) are ± 0.3 ‰ and hydrogen isotope data (δD) ± 3 ‰. Subscript in is initial and Ep stands for epidote.

Locality	Sample	U–Pb age	$^{207}Pb/^{206}Pb_{in}$	$^{87}Sr/^{86}Sr_{in}$	$\delta^{18}O_{Ep}$ [‰]	$\delta^{18}O_{Fluid}$ [‰]	δD_{Ep} [‰]	δD_{Fluid} [‰]
Grimsel test site (Grimsel Pass area)	P1[1]	278 ± 29 Ma	0.8296 ± 0.0028	0.710753 ± 0.000006	–	–	−77	−57 to −44 (200–300 °C)
	P2[1]	291 ± 50 Ma	0.8316 ± 0.0031	0.715495 ± 0.000009	–	–	−57	–
	P3[1]	275 ± 18 Ma	0.8326 ± 0.0025	–	–	–	–	–
	Grimsel-1[1,2,3]	19.2 ± 4.3 Ma	0.7964 ± 0.0027	0.726552 ± 0.000007	6.5	6.9–7.8	−55	−14 to −5 (400–600 °C)
	Grimsel-2[1,2]	16.9 ± 3.7 Ma	0.7998 ± 0.0054	–	–	–	–	–
	P6b	27.7 ± 3.4 Ma	0.7845 ± 0.0014	–	–	–	–	–
	P8	25.6 ± 4.0 Ma	0.7811 ± 0.0016	–	–	–	–	–
Gelmersee	GE4	17.8 ± 4.0 Ma	0.7308 ± 0.0032	–	–	–	–	–
Oberaletschütte	OBA19-03B	13.0 ± 1.7 Ma	0.8118 ± 0.0016	0.727619 ± 0.000007	9.4	9.8–10.7	−86	−45 to −36 (400–600 °C)
Gasterntal	GAS19-01A	13.1 ± 6.9 Ma	0.8381 ± 0.0017	0.726957 ± 0.000007	7.9	8.3–9.2	−97	−56 to −47 (400–600 °C)
Planggenstock	Planggenstock	12.4 ± 1.9 Ma	0.8071 ± 0.0011	0.710868 ± 0.000008	4.4	3.4–5.7	−104	−70 to −54 (300–600 °C)

[1] Peverelli et al. (2022a). [2] Peverelli et al. (2021). [3] Peverelli et al. (2022b).

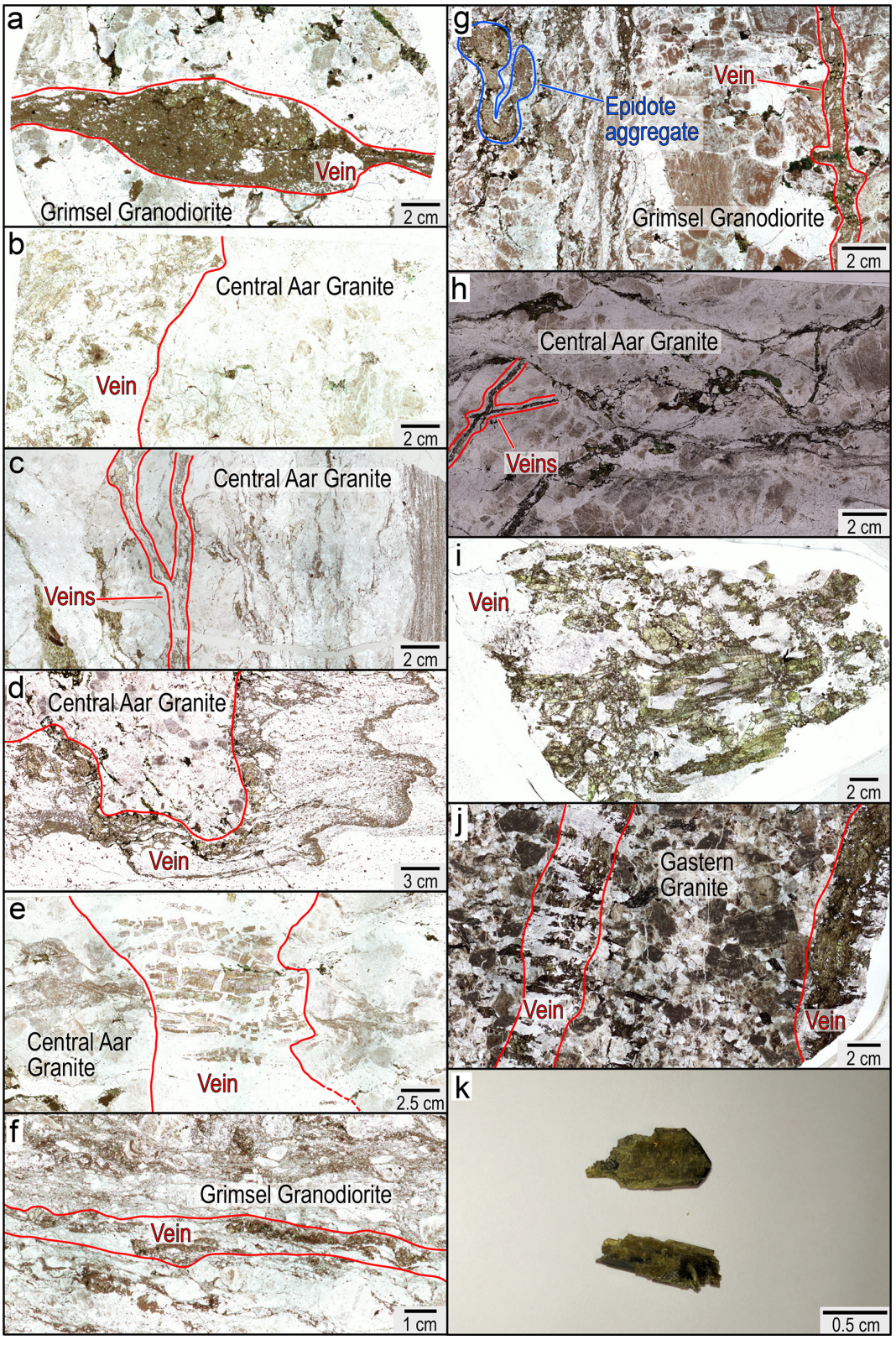

Figure 2. Transmitted-light photomicrographs of the Permian samples **(a)** P1, **(b)**, P2 and **(c)** P3; the Miocene ones **(d)** Grimsel-1, **(e)** Grimsel-2, **(f)** P6b, **(g)** P8, **(h)** GE4, **(i)** OBA19-03B, and **(j)** GAS19-01A; and a photograph of **(k)** handpicked Planggenstock epidote grains. Red curves indicate boundaries between veins and host rock. Panels **(a)**–**(c)** are modified from Peverelli et al. (2022a); **(d)**–**(e)** are modified from Peverelli et al. (2021). All thin section scans **(a–j)** are in plane-polarized light.

GTS, where sample P1 (see Sect. 3.2) was also collected (see Fig. A2 in this work and Figs. S1–S2 in Peverelli et al., 2022a). Vein P6b (Fig. 2f) is hosted by variably deformed Grimsel granodiorite. In this sample, epidote forms elongate aggregates of several epidote grains (ca. 5–200 µm) that are aligned with the foliation of the mylonitic host rock. Epidote displays lobate grain boundaries, and epidote aggregates are associated with quartz that dynamically recrystallized by sub-grain rotation recrystallization (SGR) and with green biotite. Epidote grains are weakly zoned in backscattered electron (BSE) images (Fig. 3f). Epidote in sample P8 (Fig. 2g) forms a quasi-straight vein with sharp boundaries in a weakly deformed portion of the Grimsel granodiorite and consists of mostly subhedral epidote (ca. 20–400 µm). However, the thin section includes a mylonitic portion of the host rock, in which epidote forms irregularly shaped aggregates (Fig. 2g), which were not analyzed in the present study. Epidote is only weakly zoned in BSE images in both microstructural domains (Fig. 3g). Sample GE4 (Fig. 2h) was collected north of the Grimsel Pass area, close to Gelmer Lake (Fig. 1). Epidote grains (ca. 20–500 µm) define veinlets crosscutting a weakly deformed sample of Central Aar granite. The veins are made of epidote and quartz. The subhedral epidote grains display concentric, complex, and sector zoning in BSE images (Fig. 3h). Sample OBA19-03B (Fig. 2i) is an epidote–feldspar–quartz (with minor biotite) vein sampled in the Oberaletschhütte area (close to Aletsch Glacier, Central Aar Massif; Fig. 1) and hosted by the Central Aar granite, with epidote grains ranging from 10 µm up to 5 mm. Epidote grains are mostly euhedral to subhedral, and they are highly zoned in BSE images, displaying mostly concentric or sector zoning (Fig. 3i). Sample GAS19-01A (Fig. 2j) is an epidote vein hosted by the Gastern granite and collected in the Gastern Valley (western Aar Massif; Fig. 1). Epidote grains measure ca. 20–500 µm, and they are mostly euhedral to subhedral. Epidote displays sector, concentric, and patchy chemical zoning in BSE images (Fig. 3j). Minor quartz and biotite are associated with epidote in this vein. Epidote sample Planggenstock (Fig. 2k) is from a meter-sized cleft, forming part of the > 50 m long Planggenstock cleft system in the canton of Uri (eastern Aar Massif; Fig. 1), located in the Central Aar Granite. Epidote is associated with decimeter-sized quartz crystals, small adularia, crystals and chlorite. Euhedral epidote grains reach ca. 2 cm in length. Epidote grew on an older generation of quartz and is partially overgrown by a younger generation of quartz. Epidote is fractured and displays weak patchy zoning in BSE images (Fig. 3k).

3.2 Previously published samples

Epidote veins P1, P2, and P3 are described in detail in Peverelli et al. (2022a), sample Grimsel-1 in Peverelli et al. (2021, 2022b), and sample Grimsel-2 in Peverelli et al. (2021). Epidote vein P1 (Fig. 2a) is an epidote–quartz vein sampled in a weakly deformed portion of the Grimsel granodiorite. Epidote grains measure ca. 20–300 µm and display regular chemical zoning in BSE images (Fig. 3a). Quartz is dynamically recrystallized by SGR. Vein P2 (Fig. 2b) is an epidote–quartz–feldspar vein in weakly deformed Central Aar granite. Epidote ranges between 50 µm and 2 mm, and quartz is dynamically recrystallized by SGR. Importantly, epidote in vein P2 presents microstructural (Fig. 3b) and isotopic evidence for post-crystallization fluid–mineral interaction (see Peverelli et al., 2022a). This implies that bulk Sr and H isotope measurements (see Methods and Results) represent variably mixed signals between epidote relicts and recrystallized domains, while in situ U–Pb isotope measurements only targeted non-recrystallized domains, as outlined in Peverelli et al. (2022a). The deformed vein P3 (Fig. 2c), consisting of epidote and quartz dynamically recrystallized by SGR, cuts a weakly deformed portion of the Central Aar granite. Epidote grains measure ca. 20–150 µm and display regular chemical zoning in backscattered electron images (Fig. 3c). Epidote vein Grimsel-1 (Fig. 2d) is a folded epidote–quartz–biotite vein in weakly deformed Central Aar granite, with epidote grains measuring ca. 5–200 µm, and chemical zoning is revealed by BSE images (Fig. 3d) and electron probe microanalysis (EPMA) chemical maps (Fig. 10 in Peverelli et al., 2022b). Epidote in this vein underwent dissolution–precipitation processes during vein deformation, with the fluid that mediated dissolution–precipitation including an external component with different Pb and Sr isotope ratios (Peverelli et al., 2022b). Epidote vein Grimsel-2 is an epidote–quartz–biotite vein cutting a weakly deformed portion of the Central Aar granite, containing epidote grains ranging from a few micrometers to 3 mm in size. The associated quartz is dynamically recrystallized by SGR. Backscattered electron images reveal regular chemical zoning in epidote grains (Fig. 3e).

4 Methods

The samples were characterized by optical microscopy using a ZEISS Axioplan microscope and a Zeiss EVO50 scanning electron microscope (SEM; ca. 1 nA beam current, 20 kV acceleration voltage, and working distances of 8.0–10.0 mm). All measurements were carried out in the laboratory facilities of the Institute of Geological Sciences of the University of Bern, Switzerland, unless specified otherwise. Mass fractions of Pb, Th, U, and the total sum of rare-earth elements (ΣREE), as well as a description of the LA-ICP-Ms systems and protocols for measurements, are presented in the Supplement (Table S4).

4.1 Epidote U–Pb geochronology by LA-ICP-MS

Measurements of U–Pb isotope data for epidote geochronology were performed on a RESOlutionSE 193 nm ArF excimer laser system (Applied Spectra, USA) combined with an Agilent 7900 ICP-QMS. The analytical protocol pre-

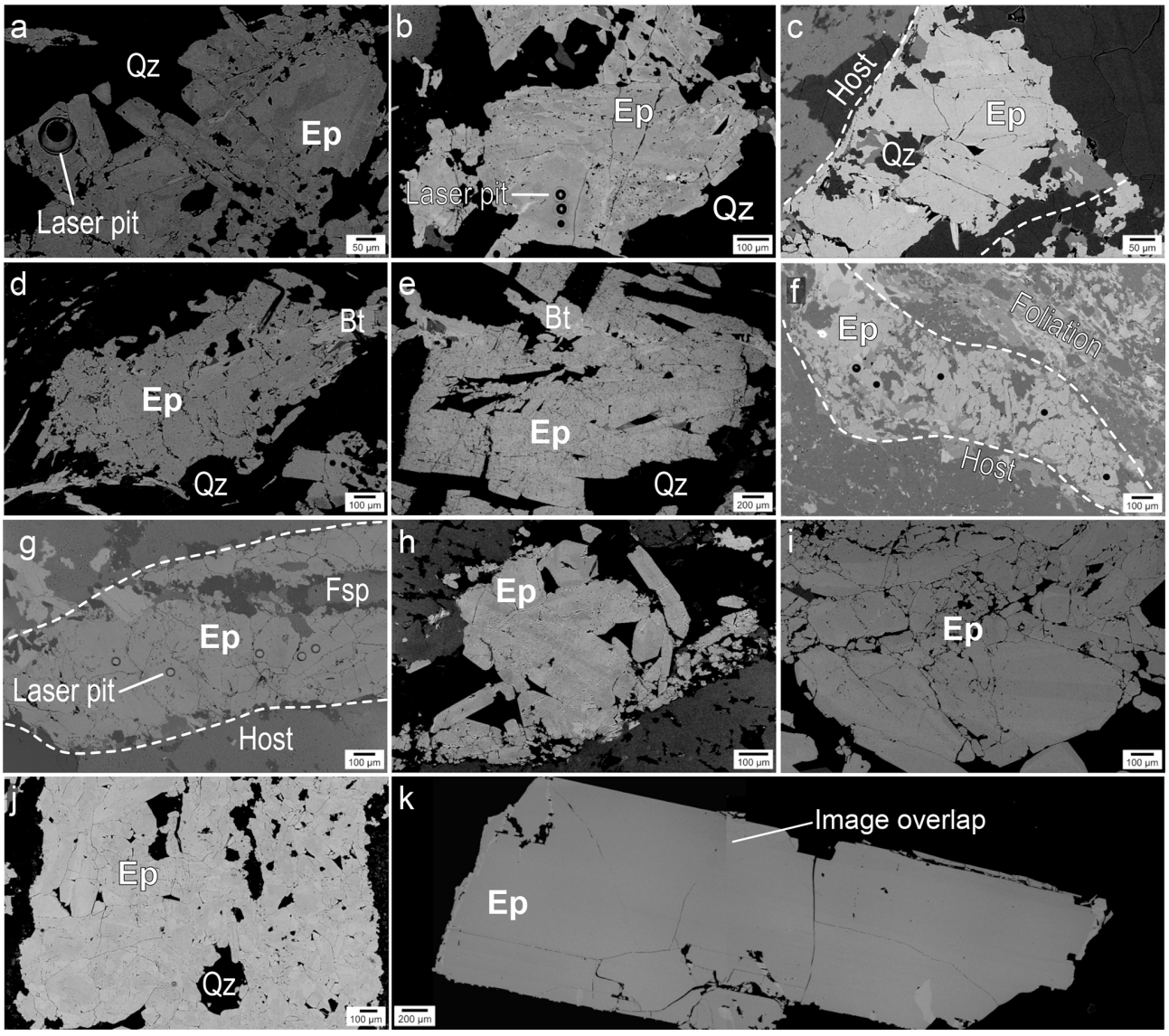

Figure 3. Backscattered electron images of Permian epidote samples **(a)** P1, **(b)** P2, and **(c)** P3 (modified from Peverelli et al., 2022a); Miocene samples **(d)** Grimsel-1, **(e)** Grimsel-2, **(f)** P6b, **(g)** P8, **(h)** GE4, **(i)** OBA19-03B, **(j)** GAS19-01A; and **(k)** Planggenstock (handpicked grain in epoxy mount). Dashed white curves indicate the boundaries between veins and host rocks. Bt is biotite, Ep is epidote, Fsp is feldspar, and Qz is quartz.

sented in Peverelli et al. (2021) was employed, using Tara allanite (Gregory et al., 2007; Smye et al., 2014) as a primary reference material with the reference isotope ratios given in Table 2 of Peverelli et al. (2021). All ages are reported with their uncertainty at a 95 % confidence level. Allanite samples CAP and AVC (Barth et al., 1994; Gregory et al., 2007) were used as secondary reference materials for quality control, and they returned ages consistent with, or sufficiently close to, their published reference U–Pb ages (Fig. A1). Data reduction was carried out in Iolite (version 7.08) using the VisualAge_UcomPbine data reduction scheme (Chew et al., 2014), and the correction for downhole fractionation, modeled on the Tara allanite primary reference material, was applied using an exponential function. The analysis spots were planned using BSE images. Detailed results of secondary reference materials are in the Supplement. Analytical conditions, U–Pb isotope data of secondary reference materials, and epidote unknowns are in the Supplement (Tables S1 and S2–S3).

4.2 Initial Sr isotope data of epidote

Strontium isotope data of epidote were measured on a ThermoFisher Triton thermal ionization mass spectrometer (TIMS) on ground epidote separates, which were dissolved

in distilled acids. Circa 1–4 mg of epidote material, matching ca. 250 ng of Sr, was dissolved in concentrated HF : HNO_3 (3 : 1 by volume). Along with epidote separates, standards AGV-2 and GSP-2 (Weis et al., 2006) and blanks were also prepared following the same procedure as that described for epidote micro-separates. The Sr fraction was purified from the rock matrix by ion chromatography employing a Sr-specTM resin (Horwitz et al., 1992) redissolved in 1 µL of 6M HCl and loaded on Re filaments using 1.5 µL Ta-oxide activator. The SRM 987 (Weis et al., 2006) was also loaded on filaments and analyzed for quality control, yielding a $^{87}Sr/^{86}Sr$ of 0.710279 ± 0.000020 (2 standard deviations, SD; number of replicates, $n = 12$). Within-run instrumental mass fractionation was corrected for using the International Union of Pure and Applied Chemistry (IUPAC) $^{88}Sr/^{86}Sr$ ratio of 8.735209, and the interference of ^{87}Rb on ^{87}Sr was corrected for using the IUPAC $^{87}Rb/^{85}Rb$ ratio of 0.385617. Because epidote incorporates negligible amounts of Rb (e.g., Frei et al., 2004), the measured $^{87}Sr/^{86}Sr$ ratios are the Sr isotope compositions of Sr incorporated by epidote during crystallization and reflect the isotope composition of Sr transported by the epidote-forming fluids. The $^{87}Sr/^{86}Sr$ values of host granitoids and shear zones (see Sect. 5.2 and Fig. 5) were calculated from the published Rb–Sr data (Schaltegger, 1990; Challandes et al., 2008) from 300 Ma (i.e., the time of pluton emplacement) and 25 Ma, respectively (i.e., the oldest shear zone in Challandes et al., 2008), until 10 Ma.

4.3 Hydrogen and oxygen isotope data

Oxygen and hydrogen stable isotope data are reported as δD and $\delta^{18}O$ per mille values [‰], respectively, relative to the Vienna Standard Mean Ocean Water (VSMOW). Hydrogen isotope ratios were measured using ca. 4 mg of ground epidote at the Goethe University–Senckenberg BiK-F Joint Stable Isotope Facility (Frankfurt, Germany) using a high-temperature conversion elemental analyzer (TC/EA) coupled to a Thermo MAT 253 mass spectrometer in continuous flow mode. The standards USGS57 (biotite), USGS58 (muscovite), NBS22 (oil), and CH7 (polyethylene foil) were used for quality control and gave δD values of −28.4 ‰, −91.9 ‰, −100.0 ‰, and −116.9 ‰, respectively, after correction for instrumental mass fractionation, daily drift of the thermal combustion reactor, and offset from the certified reference. The in-house standard "epidote_1867m" (Bird et al., 1988) gave a δD of −95 ‰. The δD values of epidote-forming fluids were calculated following Chacko et al. (1999; fractionation factors epidote–water) from measurements in ground epidote material.

Measurements of oxygen isotope data were carried out on single epidote grains using a CO_2-laser extraction line and fluorination coupled to a Finnigan MAT 253 mass spectrometer at the University of Lausanne (Switzerland). Details of the procedure are in Lacroix and Vennemann (2015). A total of three CO_2-laser fluorination sessions were carried out. All results were corrected to session values of the in-house quartz standard LS-1. Daily replicates of the LS-1 quartz standard are better than 0.1 ‰ (1 SD); deviation from the accepted $\delta^{18}O$ value of 18.1 ‰ is better than 0.2 ‰ (1 SD). Unknown replicates are within 0.3 ‰ (1 SD) or better. The $\delta^{18}O$ values of epidote-forming fluids were calculated following Zheng (1993; epidote–water fractionation) from measurements in epidote grains.

5 Results

A summary of U–Pb ages and Pb–Sr–O–H isotope data is presented in Table 1. U–Pb isotope measurement data of epidote unknowns are reported in the Supplement (Table S3).

5.1 Epidote U–Pb geochronology

Epidote in sample P6b gave a lower intercept of 25.1 ± 7.2 Ma with a very high mean-square-of-weighted-deviates (MSWD) value of 14 ($n = 25$) and an initial $^{207}Pb/^{206}Pb$ ratio of 0.7835 ± 0.0012 (not shown in Table 1 and Fig. 4). The data points not crossing the error envelope were inspected in BSE images. Although some analyses displayed no textural features (chemical zoning, grain porosity, solid or fluid inclusions, etc.) that suggest that these data points should be discarded, some measurements were placed very close to grain boundaries (possibly analyzing the bordering mineral in depth) or to mineral inclusions, which may be the cause of the scatter around the Tera–Wasserburg regression. Therefore, we removed the analyses not fitting the regression to obtain a more statistically robust lower intercept. If the data points not crossing the error envelope (outliers, spots 5, 7, 9, 12, 14, 21, 23, and 24; Table S3 and red data points in Fig. 4a) are excluded from the regression, a lower intercept of 27.7 ± 3.4 Ma is obtained, with an MSWD value of 2.7 ($n = 17$) and an initial $^{207}Pb/^{206}Pb$ ratio of 0.7845 ± 0.0014 (Table 1). After excluding the outliers, the calculated age and initial $^{207}Pb/^{206}Pb$ ratio remain within the uncertainty of those calculated from the whole dataset. Epidote in sample P8 returned a lower intercept of 25.6 ± 4.0 Ma (MSWD = 2.2; number of analyses, $n = 20$) with an initial $^{207}Pb/^{206}Pb$ ratio of 0.7811 ± 0.0016 in a Tera–Wasserburg diagram (Fig. 4b). Epidote in sample GE4 gave a lower intercept of 17.2 ± 8.1 Ma with a high MSWD value of 12 ($n = 24$) and with an initial $^{207}Pb/^{206}Pb$ ratio of 0.7291 ± 0.0024 (not shown in Table 1 and Fig. 4). By excluding the data points that do not cross the error envelope (red data points in Fig. 4c and spots 1, 2, 5, 17, 18, and 24 in Table S3), following the same rationale outlined for sample P6b, the lower intercept obtained is 17.8 ± 4.0 Ma (MSWD = 2.2; $n = 18$; Fig. 4c) with an initial $^{207}Pb/^{206}Pb$ ratio of 0.7308 ± 0.0032 (Table 1). Also in this case, age and the initial $^{207}Pb/^{206}Pb$ ratio calculated from the dataset excluding outliers remain within the uncertainty range of those calcu-

lated from the entire dataset. Epidote in sample OBA19-03B yielded a lower intercept of 13.0 ± 1.7 Ma (MSWD = 2.2; $n = 19$; Fig. 4d) with an initial $^{207}Pb / ^{206}Pb$ ratio of 0.8118 ± 0.0016. Epidote vein GAS19-01A gave a lower intercept of 13.1 ± 6.9 Ma (MSWD = 1.5; $n = 28$; Fig. 4e) with an initial $^{207}Pb / ^{206}Pb$ ratio of 0.8381 ± 0.0017. Epidote from the Planggenstock cleft yielded a lower intercept of 12.4 ± 1.9 Ma (MSWD = 1.4; $n = 36$, measured in two separate grains; Fig. 4f) with an initial $^{207}Pb / ^{206}Pb$ ratio of 0.8071 ± 0.0011.

As for the previously published samples, epidote P1, P2, and P3 gave Permian ages of 278 ± 29 Ma (MSWD = 2.0; $n = 36$) with an initial $^{207}Pb / ^{206}Pb$ ratio of 0.8296 ± 0.0028, 291 ± 50 Ma (MSWD = 2.0; $n = 24$) with an initial $^{207}Pb / ^{206}Pb$ ratio of 0.8316 ± 0.0031, and 275 ± 18 Ma (MSWD = 2.3; $n = 17$) with an initial $^{207}Pb / ^{206}Pb$ ratio of 0.8326 ± 0.0025, respectively (Peverelli et al., 2022a). It should be noted here that LA-ICP-MS is an in situ technique, ensuring that the initial $^{207}Pb / ^{206}Pb$ ratio of sample P2 reflects non-recrystallized epidote because recrystallized domains were not measured by Peverelli et al. (2022a). Sample Grimsel-1 gave a Miocene age of 19.2 ± 4.3 Ma (MSWD = 0.79; $n = 23$) with an initial $^{207}Pb / ^{206}Pb$ ratio of 0.7964 ± 0.0027 and sample Grimsel-2 another Miocene age of 16.9 ± 3.7 Ma (MSWD = 0.4; $n = 16$) with an initial $^{207}Pb / ^{206}Pb$ ratio of 0.7998 ± 0.0054 (Peverelli et al., 2021).

5.2 Strontium isotope data

Strontium isotope ratios could not be measured in Permian sample P3 and in Miocene samples Grimsel-2, P6b, P8, and GE4 due to an insufficient amount of sample material available to ensure enough Sr for isotope analysis by TIMS. Permian samples P1 and P2 gave $^{87}Sr / ^{86}Sr$ ratios (with uncertainties as 2 standard errors, 2 SE) of 0.710753 ± 0.000006 and 0.715495 ± 0.000009, respectively. Miocene epidote OBA19-03B and GAS19-01A yielded $^{87}Sr / ^{86}Sr$ ratios of 0.727619 ± 0.000007 and 0.726957 ± 0.000007, respectively. Finally, epidote cleft sample Planggenstock returned a $^{87}Sr / ^{86}Sr$ ratio of 0.710868 ± 0.000008. The $^{87}Sr / ^{86}Sr$ ratio of epidote in sample Grimsel-1 is published in Peverelli et al. (2022b), who determined that epidote underwent dissolution–precipitation processes and that this late fluid had a Sr isotope composition different than the fluid present during epidote vein formation. Non-recrystallized epidote has a $^{87}Sr / ^{86}Sr$ ratio of 0.726552 ± 0.000007, while the $^{87}Sr / ^{86}Sr$ ratios of mixtures with variable and unknown amounts of recrystallized epidote vary between 0.726830 ± 0.000015 and 0.727807 ± 0.000007. Because the exact Sr isotope composition of recrystallized Grimsel-1 epidote could not be determined (see Peverelli et al., 2022b), we use the $^{87}Sr / ^{86}Sr$ ratio of non-recrystallized epidote for further discussion.

Plotting the Sr isotope ratios of the epidote samples studied against the ages obtained by U–Pb geochronology (Fig. 5) reveals that the Sr isotope ratios of Permian samples P1 and P2 are more radiogenic than those of their host rocks (Central Aar Granite and Grimsel Granodiorite; Schaltegger, 1990). The $^{87}Sr / ^{86}Sr$ ratio of sample P2, bearing evidence of fluid–mineral interaction processes (see Sect. 3.2), plots between the value of sample P1 and more radiogenic values of some Miocene samples. Miocene epidote samples Grimsel-1, OBA19-03B, GAS19-01A, and Planggenstock plot within the field defined by the $^{87}Sr / ^{86}Sr$ ratios of host granitoids (Schaltegger, 1993) and the shear zones (Challandes et al., 2008) calculated at the time of vein formation. Even higher $^{87}Sr / ^{86}Sr$ data were measured in shear zones by Marquer and Peucat (1994), expanding the shear zone field to even more radiogenic values, corroborating the finding that the $^{87}Sr / ^{86}Sr$ ratios of Miocene epidote samples plot well within the field of values measured in the Alpine shear zones. It should be noted that Fig. 5 does not include the $^{87}Sr / ^{86}Sr$ data measured in granitoids by Dempster (1986), since these data, although considered in the discussion, likely show disturbance of the Rb–Sr isotope system during rejuvenation of the granitoids and minerals therein in Alpine times. Therefore, in a $^{87}Sr / ^{86}Sr$ vs. age diagram, it would be inaccurate to plot initial $^{87}Sr / ^{86}Sr$ without reliable age-dependent corrections for radiogenically ingrown ^{87}Sr. To our knowledge, no Sr isotope data exist for the Gastern Granite, precluding a comparison with the $^{87}Sr / ^{86}Sr$ ratios of sample GAS19-01A.

5.3 Hydrogen and oxygen isotope data

New hydrogen isotope data (expressed as δD, all ± 3 ‰; Table 1) were obtained from Miocene samples OBA19-03B (−86 ‰), GAS19-01A (−97 ‰), and Planggenstock (−104 ‰), and they will be used in combination with δD values of samples P1 (−77 ‰), P2 (−59 ‰), and Grimsel-1 (−55 ‰) from Peverelli et al. (2022a). New oxygen isotope ratios (expressed as $\delta^{18}O$, all ± 0.3 ‰) from samples Grimsel-1, GAS19-01A, and Planggenstock are 6.5 ‰, 9.4 ‰, 7.9 ‰, and 4.4 ‰, respectively (Table 1).

The δD and $\delta^{18}O$ values of the epidote-forming fluids can be calculated by defining the temperature range of epidote crystallization, using the epidote–water fractionation factors of Chacko et al. (1999) for δD and Zheng (1993) for $\delta^{18}O$ values. A closed system can be assumed for Permian epidote P1 and for Miocene epidote samples OBA19-03B, GAS19-01A, and Planggenstock, where no evidence for post-crystallization fluid–mineral interaction is detected. The δD value of the fluid involved in epidote P1 formation was calculated for a temperature of 250 ± 50 °C, resulting in values ranging from −57 ‰ to −44 ‰ (Peverelli et al., 2022a). In Miocene vein samples OBA19-03B and GAS19-01A, epidote coexists with minor green biotite, which is an indicator that temperatures were above 400 °C but did not

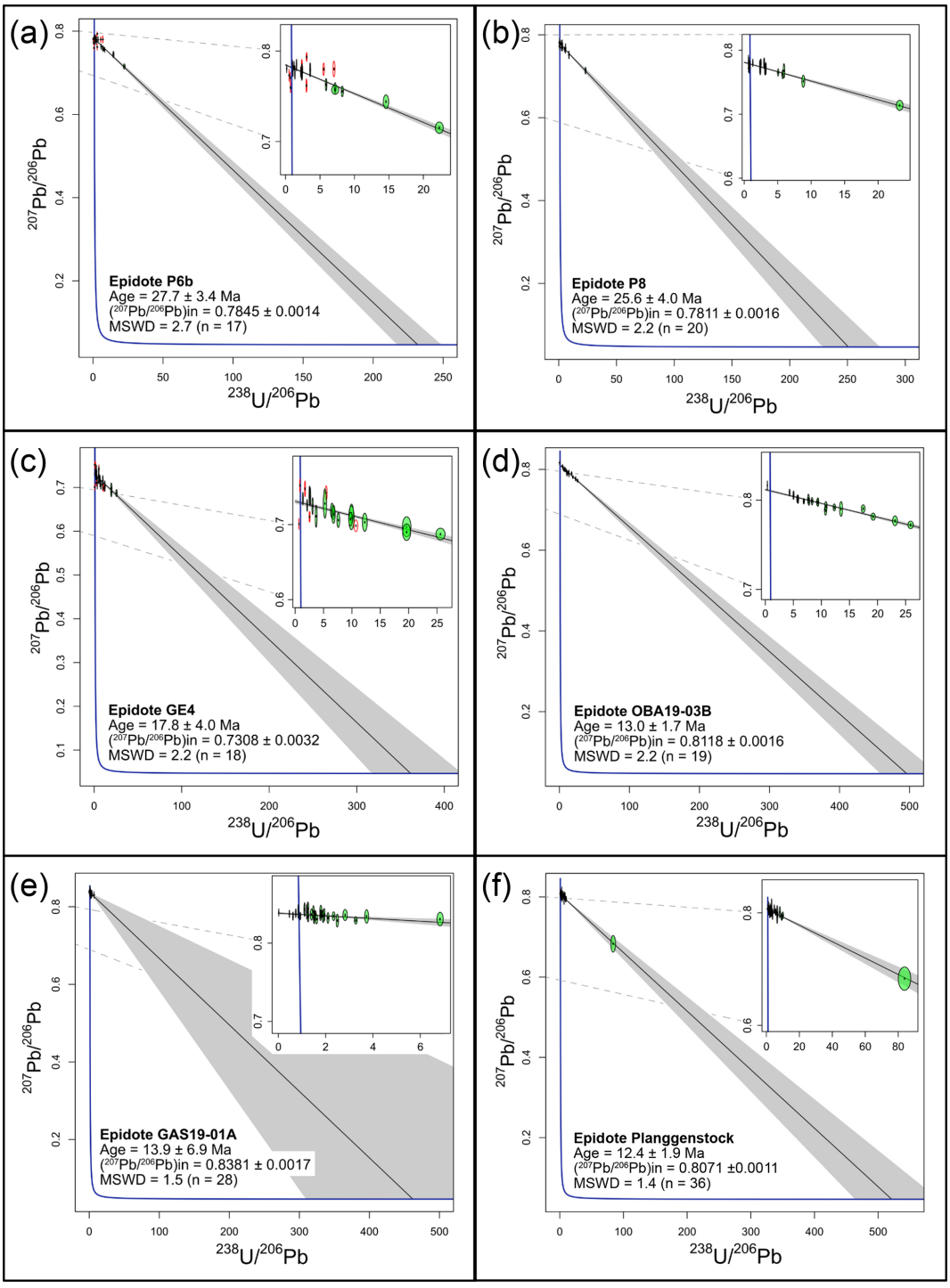

Figure 4. Tera–Wasserburg plots of epidote samples **(a)** P6b, **(b)** P8, **(c)** GE4, **(d)** OBA19-03B, **(e)** GAS19-01A, and **(f)** Planggenstock. Error ellipses are 2σ, and age uncertainties are given at a 95 % confidence level. Plotted with IsoplotR (Vermeesch, 2018). Red data points in panels **(a)** and **(c)** are the excluded analyses.

exceed 480 °C (see Goncalves et al., 2012; Wehrens et al., 2017). However, the maximum temperature to be considered for our calculations is 600 °C since we cannot ascertain whether hydrothermal fluids thermally equilibrated with their surroundings during circulation, and minerals of the epidote–clinozoisite solid solution can form up to 600 °C (see Franz and Liebscher, 2004). Therefore, the temperature range of 400–600 °C is used here for our calculations.

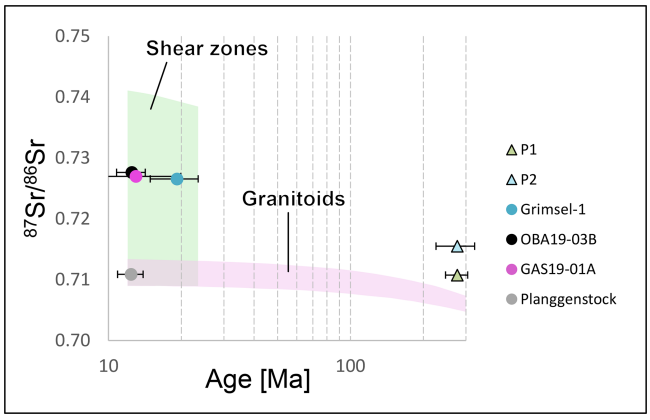

Figure 5. Strontium isotope compositions of the studied epidote samples compared to the $^{87}Sr / ^{86}Sr$ evolution of the Central Aar Granite and the Grimsel Granodiorite (from Schaltegger, 1990) and shear zones (from Challandes et al., 2008). The evolution curves were calculated from present-day measurements of Rb and Sr mass fractions and from $^{87}Rb / ^{86}Rb$ and $^{87}Sr / ^{86}Sr$ ratios in whole rock samples. The plot does not include the data of Dempster (1986; see text for details). Error bars of Sr isotope ratios are smaller than the symbols.

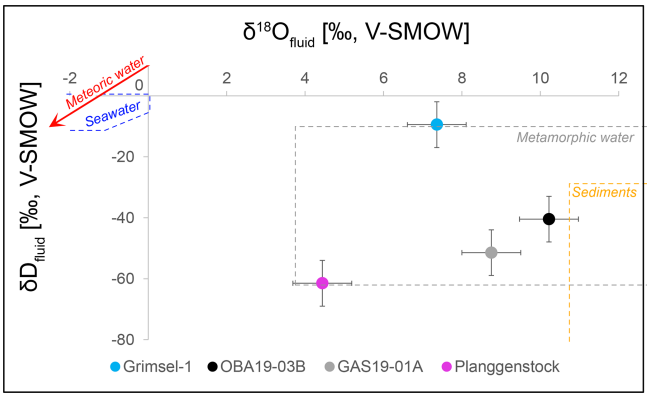

Figure 6. Stable isotope ratios of Miocene epidote-forming fluids as $\delta^{18}O$ and δD relative to the Vienna Standard Mean Ocean Water (VSMOW) calculated from measurements in epidote minerals. The global meteoric line (meteoric water) extends outside the field, as indicated by the red arrowhead according to the equation $\delta D = 8 \times \delta^{18}O + 10$. Fields of seawater and metamorphic and sedimentary waters are from Sheppard (2019).

For Planggenstock epidote, an upper temperature limit of 600 °C can also be used for the same reasons. However, because biotite is absent in the Planggenstock cleft where the sample studied was collected, we will use the lower temperature limit of greenschist-facies metamorphism (ca. 300 °C; see Sect. 2) as the minimum temperature of epidote crystallization. Thus, the calculated δD values of Miocene epidote-forming fluids (Fig. 6) are −45 ‰ to −36 ‰ for epidote OBA19-03B, −56 ‰ to −47 ‰ for epidote GAS19-01A, and −70 ‰ to −54 ‰ for epidote Planggenstock. The calculated $\delta^{18}O$ values of Miocene fluids are 6.9 ‰–7.8 ‰ (non-recrystallized epidote Grimsel-1), 9.8 ‰–10.7 ‰ (epidote OBA19-03B), 8.3 ‰–9.2 ‰ (epidote GAS19-01A), and 3.4 ‰–5.7 ‰ (epidote Planggenstock). Due to recrystallization processes in sample P2 (see Peverelli et al., 2022a), no δD value for the P2 epidote-forming fluid can be calculated since temperature conditions between epidote formation in the Permian and epidote recrystallization at unknown times cannot be assumed to have been the same. In sample Grimsel-1, epidote was affected by dissolution–precipitation processes. However, physicochemical conditions must have remained similar between vein formation and deformation, given the consistency of trace element patterns between epidote relicts and recrystallized grains (Peverelli et al., 2022b). Therefore, the use of the δD range of −14 ‰ to −5 ‰ calculated by Peverelli et al. (2022a) at temperatures of 400–600 °C can be used here.

6 Discussion

The following discussion combines geochronological and isotope data measured in hydrothermal epidote in veins to progressively reconstruct the dynamics of fluid circulation in deformed granitoids. It should be appreciated here that all interpretations are deducted from one mineral only, an approach that has successfully been applied in similar studies (Peverelli et al., 2022a, 2023). We present hypotheses regarding fluid sources and pathways and regarding the effects of fluid circulation on the deforming granitoids as a geochemical system.

6.1 Epidote U–Pb ages

6.1.1 Scattered Tera–Wasserburg diagrams

The Tera–Wasserburg regressions of epidote samples P6b and GE4 using the whole datasets returned high MSWD values caused by the scatter of several data points (Fig. 4). Successful age calculation using the Tera–Wasserburg approach relies on sufficient spread among co-varying individual spot analyses in the $^{207}Pb / ^{206}Pb$ vs. $^{238}U / ^{206}Pb$ space (i.e., Tera–Wasserburg diagram), which thus constrains the regression quality. In samples P6b and GE4, this is guaranteed by a sufficient number of analyses that have lower, although still high, fractions of initial Pb (f_{206} of 0.91–0.97 for sample P6b and 0.94–0.97 for sample GE4; see the Supplement). High MSWD values indicate scattered data points along this regression, which can be ascribed to different formation ages and/or different initial $^{207}Pb / ^{206}Pb$ ratios of individual spots. Although the present data do not allow us to untangle the exact causes, both options might be true if input of isotopically different Pb occurred during vein formation

or if new epidote with different initial $^{207}Pb/^{206}Pb$ precipitated during fluid-assisted deformation of epidote veins. In fact, variations in Pb and Sr isotope compositions of epidote during deformation by viscous granular flow were found in epidote Grimsel-1 (Peverelli et al., 2022b), allowing us to accept dissolution–precipitation processes as likely causes for the observed scatter. The variability in initial $^{207}Pb/^{206}Pb$ ratios of Miocene epidote samples (Table 1 and Fig. 4) indicates that Miocene fluids transported Pb with variable isotope compositions. Therefore, the interplay of isotopically different fluids during crystallization of epidote P6b and GE4 and consequent initial Pb isotope heterogeneity in these epidote samples may well account for the scattered data points in the Tera–Wasserburg plots (Fig. 4). The present conclusion would benefit from in situ stable isotope data, which could not be acquired for this study but which could corroborate the above.

6.1.2 Miocene epidote veins

All newly obtained ages are Miocene (Fig. 4) and consistent with the tectonic evolution of the area during the Alpine orogeny, with Alpine deformation starting ca. 25 Mya ago (Handegg phase) and continuing at least until 10.9 Ma (Oberaar phase; Challandes et al., 2008; Rolland et al., 2009; Berger et al., 2017b; Wehrens et al., 2017; Gnos et al., 2021). Our geochronological results thus indicate that formation of epidote veins lasted from maximum burial throughout the uplift of the Aar Massif to shallower crustal levels and in all sectors of the massif (Fig. 1). Miocene fluid circulation in the Aar Massif has been documented thanks to a wide variety of evidence besides epidote veins, such as quartz and monazite in clefts (Janots et al., 2012; Berger et al., 2013; Bergemann et al., 2017; Ricchi et al., 2019; Gnos et al., 2021), hydrothermal adularia and calcite veins (Rossi and Rolland, 2004), crystallization of green biotite in shear zones (Challandes et al., 2008; Rolland et al., 2009), and Sr isotope data of Miocene shear zones (Marquer and Peucat, 1994). In the Pliocene, fluid circulation continued as documented by a mineralized breccia at Grimsel Pass (central Aar Massif, where the GTS is situated; Fig. 1; Hofmann et al., 2004; Berger et al., 2022). Present-day fluid circulation of deeply infiltrated meteoric water is documented by active geothermal systems (e.g., Diamond et al., 2018). The crystallization of multiple mineral phases (i.e., epidote, monazite, and apatite; Janots et al., 2012; Berger et al., 2013; Cenki-Tok et al., 2014; Bergemann et al., 2017; Ricchi et al., 2019; Peverelli et al., 2021, 2022b; Berger et al., 2022) in the Miocene illustrates the chemical complexity of the circulating fluids. However, the history of fluid circulation in the Aar Massif began much earlier than the Miocene, as confirmed by whole rock Rb / Sr isotope data indicating fluid circulation in the Triassic or later (Abrecht and Schaltegger, 1988) and by Permian epidote veins (Peverelli et al., 2022a). The Miocene epidote veins presented here, in combination with previous work, support the hypothesis that widespread fluid circulation accompanied the whole tectonic evolution of the granitic continental crust in the Aar Massif.

6.2 Isotope data and fluid sources/pathways

Establishing the timing of vein formation permits the assessment of the isotope compositions of hydrothermal epidote with respect to (trans-)tensional Permian and Miocene compressional geodynamics. This allows us to reconstruct fluid sources and pathways that are consistent with the tectonic evolution of the granitic continental crust. Trans-tension in the Permian (Oberhänsli et al., 1988) induced a hydrogeological cycle likely controlled by surface water (e.g., meteoric, riverine, and lacustrine water). Contrastingly, Miocene compressional tectonics involved reworking, burial, and compaction of marine sediments (e.g., Mesozoic sediments, Upper Marine Molasse; see Pfiffner, 1993; Berger et al., 2017b) as potential fluid sources.

6.2.1 Permian fluids

Permian fluids were interpreted as being of meteoric origin, with the addition of a sedimentary water component resulting in fluid mixing based on geodynamic constraints and hydrogen isotope data (Peverelli et al., 2022a). Permian epidote samples P1 and P2 have more radiogenic $^{87}Sr/^{86}Sr$ ratios than their host granitoid at the time of epidote vein formation (Fig. 5). This implies that Permian fluids inherited radiogenic Sr from Rb-enriched sources, which may have been inside or outside the veins' host. Meteoric water is unlikely to carry large amounts of Sr without interacting with Sr-enriched media (i.e., lithologies, minerals, or other fluids). Possibly, radiogenic Sr was inherited from interaction of the fluids with syn-rift sedimentary units during circulation, and/or from Rb-enriched minerals (e.g., magmatic biotite) present within the Aar Massif granitoids themselves. Both hypotheses are, however, plausible and consistent with the fluid pathways proposed by Peverelli et al. (2022a; their Fig. 4), with fluids exploiting syn-rift faults for downwards percolation, thus interacting with syn-rift sediments and the fractured granitoids. The fact that Permian sample P2 includes more radiogenic Sr than coeval sample P1 may signify two things: (1) different Permian fluids transported Sr components acquired from different sources or (2) post-crystallization interaction with fluids carrying a radiogenic Sr component caused partial recrystallization of epidote P2. Given that epidote P2 bears evidence of partial recrystallization (Fig. 3b; see also Fig. 2 in Peverelli et al., 2022a), the second hypothesis is preferred here. This is supported by these samples having initial $^{207}Pb/^{206}Pb$ ratios within the uncertainty ranges of each other: while the Sr isotope composition of epidote P2 mixes recrystallized and non-recrystallized epidote portions, the use of in situ LA-ICP-MS for U–Pb isotope analyses ensures that only primary, non-recrystallized domains of epi-

dote are sampled. The consistency between the initial Pb isotope ratios of epidote samples P1 and P2 indicates that the Pb incorporated by these samples had the same origin, thus the sharing of similar sources and pathways by Permian fluids. Therefore, the more radiogenic Sr isotope composition of sample P2 was likely induced by a ^{87}Sr-enriched fluid that mediated recrystallization at unknown times. We cannot exclude the possibility that post-crystallization fluid–mineral interaction may have been mediated by Miocene fluids (see Sect. 6.2.2) or by undetected fluid circulation at other times. In fact, the occurrence of Mesozoic fluid circulation in the Aar Massif was suggested by Abrecht and Schaltegger (1988), who proposed ingression of seawater at this time. The $^{87}Sr/^{86}Sr$ ratios of Mesozoic seawater range between ca. 0.707 and 0.708 (McArthur et al., 2012). Assuming that the primary $^{87}Sr/^{86}Sr$ ratio of sample P2 was the same as that of sample P1 (0.710753 ± 0.000006), which is reasonable because these two samples have overlapping initial $^{207}Pb/^{206}Pb$ ratios, a more radiogenic fluid than pure Mesozoic seawater is required to produce the $^{87}Sr/^{86}Sr$ ratio of sample P2 (0.715495 ± 0.000009). Therefore, the hypothesis of recrystallization of epidote P2 being mediated by potentially radiogenic Alpine fluids (see below) seems more plausible.

6.2.2 Miocene fluids

Although some dated samples could not be analyzed for Sr–O–H isotopes (Sect. 5.2–5.3), the initial $^{207}Pb/^{206}Pb$ ratios of the Miocene samples that were dated indicate isotopic similarities between samples collected at the same location (e.g., samples P6b and P8 and samples Grimsel-1 and Grimsel-2; see Fig. S2) and differences among those collected at different sites. Samples Grimsel-1 and Grimsel-2 from the GTS and hosted by the Central Aar Granite show, within the uncertainty range, the same initial $^{207}Pb/^{206}Pb$ ratios, indicating that during epidote formation, fluids inherited Pb from similar sources. The same consideration is valid for initial $^{207}Pb/^{206}Pb$ ratios in samples P6b and P8, which were collected close to the same shear zone in the Grimsel Granodiorite in the GTS as the Permian sample P1. A larger range is observed in initial $^{207}Pb/^{206}Pb$ ratios of Miocene samples GE4, OBA19-03A, and Planggenstock, which are all hosted by the Central Aar Granite but were collected outside the GTS (Fig. 1). These samples show initial $^{207}Pb/^{206}Pb$ ratios ranging from 0.8118 ± 0.0016 (OBA19-03A) to 0.7308 ± 0.0032 (GE4). Sample GAS19-03A is hosted by the Gastern Granite and displays the least radiogenic initial $^{207}Pb/^{206}Pb$ ratio of all samples. Overall, initial $^{207}Pb/^{206}Pb$ ratios suggest that different fluid pathways were exploited by Miocene fluids (Fig. 7). In the following, we will address Miocene fluid sources and pathways using the Sr–O–H isotope data of the Miocene samples for which non-in-situ analyses could be carried out.

The stable oxygen and hydrogen isotope compositions of Miocene fluids calculated from measurements in epidote samples OBA19-03B, Planggenstock, and GAS19-01A (Fig. 6) plot within the field of metamorphic fluids, a term commonly used for water released by prograde metamorphic reactions (Sheppard, 2019). Such isotopic values can also be explained if meteoric water (extending to $\delta^{18}O$ and δD values from -20 ‰ to 0 ‰ and from -150 ‰ to 0 ‰, respectively; Sheppard, 2019) infiltrated and interacted with the country rock: this shifts the original δD–$\delta^{18}O$ composition of the fluid towards higher $\delta^{18}O$ values, leaving the fluid's δD value largely unaffected (Taylor, 1977, 1978). In fact, the oxygen isotope composition of all epidote-forming fluids is consistent with extensive fluid–rock interaction of such fluids with the Aar Massif granitoids (see also Rossi and Rolland, 2009). Therefore, it is likely that the calculated δD–$\delta^{18}O$ values of Miocene fluids result from interaction of meteoric water with the granitoids. Meteoric water infiltrating silicate-dominated rock units can preserve its low δD values despite isotope exchange at high temperatures (Fricke et al., 1992; Mulch and Chamberlain, 2007). The ingression of 3 myr old meteoric water in the Aar Massif to depths of ca. 10 km has been ascertained by Diamond et al. (2018), and infiltration of meteoric water down to depths of several kilometers has been documented elsewhere (e.g., Fricke et al., 1992; Mulch et al., 2004; Menzies et al., 2014; Grambling et al., 2021). However, mixing of different endmember waters is a possible occurrence as well (Fig. 7). The calculated δD values of samples OBA19-03B, GAS19-01A, and Planggenstock may be consistent with mixing of meteoric, sedimentary, and/or metamorphic water components (Fig. 6), whose involvement is expected if granitoids and sedimentary units are buried, compacted, and deformed (Fig. 7b). Mixing of water released by the devolatilization of the Helvetic schists with meteoric water in the Aar Massif has been proposed by Rossi and Rolland (2004) based on C, O, and H isotope data. Accordingly, the present epidote δD–$\delta^{18}O$ values can be explained by meteoric water infiltrating the Aar Massif granitoids along steeply oriented discontinuities (e.g., shear zones or brittle fractures), thus mixing with fluids being expelled from sedimentary units (e.g., Helvetic schists) being buried and compacted during Alpine deformation and mixing with variable amounts of fluids released during metamorphic reactions (e.g., dissolution of biotite in granitic shear zones). Such a hypothesis would best account for the observed δD values of Miocene epidote, while the observed $\delta^{18}O$ values would be explained by oxygen isotope exchange of the fluid(s) with the host granitoids. Moreover, it would be consistent with all epidote samples having more-radiogenic $^{87}Sr/^{86}Sr$ ratios than the host granitoid at the time of epidote formation (Fig. 5) – with the notable exception of Planggenstock epidote that has a lower $^{87}Sr/^{86}Sr$ ratio overlapping with its host rock. Metamorphic and sedimentary fluids are expected to inherit fair amounts of radiogenic Sr from their sources if these contain abundant Rb-rich minerals such as micas. In-

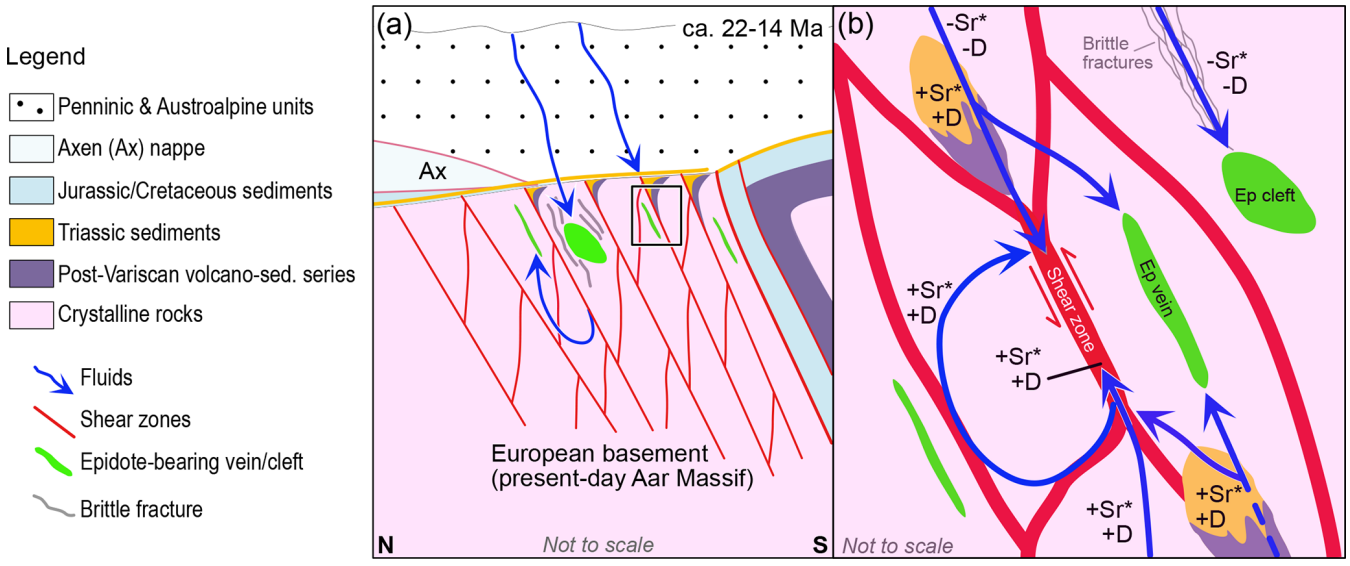

Figure 7. Schematic of Miocene fluid circulation in the Aar Massif. **(a)** Large-scale cross-section redrawn from Herwegh et al. (2020); the black rectangle shows the hypothetical location of panel **(b)**. **(b)** Zoomed-in sketch of fluid circulation across the different Sr and H reservoirs within the deforming Aar Massif granitoids. For clarity, the sketch assumes isotopic equilibration of O with the granitoids and overlooks isotopic heterogeneities in initial Pb isotope ratios (see text for details). Sr* is radiogenic Sr, and D is deuterium. Not to scale.

deed, the granite cleft wall at Planggenstock is porous due to dissolution, as observed in the field. In such a scenario, the much-less radiogenic Sr isotope composition of epidote Planggenstock can be explained by a smaller ratio between metamorphic/sedimentary and meteoric water components in its precipitating fluid. The hypothesis of meteoric water mixing with sedimentary and/or metamorphic water components can be reconciled with the Miocene tectonic evolution of the Aar Massif when one considers that Alpine shear zones can represent Variscan shear zones and/or Mesozoic extensional faults being reactivated during Alpine collision (e.g., Buehler et al., 2022; Musso Piantelli et al., 2022; Schwartz et al., 2024). Therefore, lenses of Permian and Mesozoic sediments deposited in half-grabens are likely to be reworked, buried, and compacted within Miocene shear zones (Fig. 7; see also Herwegh et al., 2020; Musso Piantelli et al., 2022). In this respect, it is possible that the fluids forming the veins Grimsel-1, OBA19-03B, and GAS19-03A exploited ductile shear zones for circulation inheriting radiogenic Sr and δD values overlapping with metamorphic and sedimentary water, while the one(s) that formed the Planggenstock cleft used a different kind of discontinuity – such as newly formed brittle fractures that were not ^{87}Sr enriched and that produced the lightest and most-meteoric-like δD value – in relatively undeformed portions of the granitoids (Fig. 7).

6.2.3 Seawater influx/recycling in the Miocene?

Miocene epidote Grimsel-1 has δ^{18}O and ^{87}Sr / ^{86}Sr values similar to all other Miocene samples (Fig. 5), while its δD value is strikingly different and has a high value that overlaps with seawater (Fig. 6). The deposition times of the Burdigalian Upper Marine Molasse north of the Grimsel Pass area (see, e.g., Schlunegger et al., 1997) overlap with the Handegg phase and the formation of Miocene epidote veins. Thus, we cannot exclude the possibility that seawater was tapped by Miocene shear zones, although such a hypothesis is highly speculative. An alternative explanation is that previously stored seawater was released from buried marine sedimentary units (e.g., Mesozoic sediments; see, e.g., Herwegh et al., 2020; 2023; Musso Piantelli et al., 2022). It has been shown that in sample Grimsel-1, interaction with an external fluid during deformation led to epidote recrystallization by dissolution–precipitation (Peverelli et al., 2022b), and this epidote sample has a δD value of -14‰ to -5‰ that is consistent with the addition of a seawater component. The present data do not allow us to conclude whether (recycled) seawater mixed with the Grimsel-1 epidote-forming fluid during vein formation or if it was introduced into the vein system during deformation as an external fluid component assisting dissolution–precipitation processes of epidote. However, the fact that trace element patterns of primary vein epidote and reprecipitated epidote are similar (see Fig. 11 in Peverelli et al., 2022b) seems to argue in favor of different fluids mixing and homogenizing before vein formation and that a similarly homogenized fluid assisted epidote dissolution–precipitation. Because epidote Grimsel-1 is the only Miocene sample available for bulk isotope measurements from the Grimsel test site, it cannot be concluded here whether this sample is isotopically unique or whether this stable isotope composition is representative of all Miocene epidote in this specific sector of the Aar Massif.

6.3 Effects of syn-orogenic fluids on the Sr isotope budget of deforming granitoids

The Sr isotope compositions of all Miocene samples plot within the calculated isotopic evolution curve of the Central Aar Granite and the Grimsel Granodiorite and within a field defined by Sr isotope data of Alpine shear zones (Fig. 5). In the case of an external origin of radiogenic Sr, the role of syn-orogenic fluids in altering the primary Sr isotope composition of the Aar Massif granitoids can be discussed considering previous work. As shown by Marquer and Peucat (1994), the Sr isotope composition of Alpine (i.e., Miocene) shear zones is determined by new mineral phases crystallizing therein and fixing external, more-radiogenic Sr in the system. In this respect, the fluids that formed the epidote samples studied may have contributed to imprinting a more-radiogenic Sr isotope composition onto the shear zones along which they circulated and within which epidote is commonly found (e.g., Wehrens et al., 2016, 2017; Schneeberger et al., 2019). It is also possible that Miocene fluids infiltrated the shear zones and assisted the formation of ^{87}Sr-enriched biotite therein. In fact, Dempster (1986) discusses the rejuvenation of the Aar Massif granitoids in the Grimsel Pass area by means of Alpine fluids related to metamorphism of the granitoids and presents highly radiogenic present-day $^{87}Sr/^{86}Sr$ ratios (see their Table 1). Although a disturbed Rb–Sr isotope system may not be reliable for calculations of initial $^{87}Sr/^{86}Sr$, such ratios vary between ca. 0.708 and 0.78 (Dempster, 1986; their Fig. 5). The fact that the $^{87}Sr/^{86}Sr$ ratios of the epidote samples studied plot within the values of undeformed granitoids (Schaltegger, 1990), shear zones (Challandes et al., 2008), and rejuvenated granitoids (Dempster, 1986) allows for the possibility that fluid circulation related to epidote vein formation contributed to the overall Sr isotopic alteration of these granitoids. On the other hand, it is also possible that fluids leached radiogenic Sr from the shear zones themselves rather than adding it. This is possible if fluid-assisted deformation caused partial dissolution of Rb-rich minerals such as biotite in the shear zones and caused the release of radiogenic Sr into the fluids. Such an alternative interpretation is also consistent with the present Sr, O, and H isotope data. Both scenarios are consistent with proposed Miocene fluid pathways (Fig. 7 and Sect. 6.2.2). It is possible that a feedback process persisted during fluid circulation (Fig. 7b): a first stage of fluid circulation driven by ^{87}Sr-enriched fluids (e.g., containing larger sedimentary and/or metamorphic water components) imprinted a more-radiogenic Sr isotope composition onto shear zone-forming minerals; the same ^{87}Sr-enriched minerals were then dissolved in a second phase of fluid circulation, where fluids were less enriched in ^{87}Sr (e.g., being more meteoric water dominated) and became enriched in radiogenic Sr only by interacting with the shear zones. Such a hypothesis can explain Pb–Sr–H isotopic differences among Miocene samples (Figs. 5–7), which allows for the hypothesis that multiple fluid pathways were exploited by the Miocene fluids. This highlights the importance of future work addressing the interplay of shear zones and circulating fluids during orogeny and the role of shear zones as fluid conduits.

7 Conclusions and outlook

We have presented U–Pb geochronological data of epidote in hydrothermal veins collected at several localities in the Aar Massif, which showed Miocene ages consistent with the tectono-metamorphic history of the Alpine orogen in the area. The obtained ages, in combination with previous work, show that epidote formation accompanied the evolution of the granitic continental crust in the inverted European passive continental margin with a gap in the Mesozoic. We have presented evidence that Miocene fluid sources and fluid pathways in the Aar Massif were complex, with the possible mixing of three endmember waters (i.e., meteoric, metamorphic, and sedimentary fluids). Finally, our Sr isotope data offer two possible interpretations: (1) the fluids transported radiogenic Sr into the shear zones, contributing to the high-Sr-isotope composition of shear zone rocks and metamorphic biotite consistent with previous studies, or (2) the fluids inherited radiogenic Sr by exploiting shear zones for circulation and leaching Sr from rocks and the biotite therein, characterized by high $^{87}Sr/^{86}Sr$ ratios. Both scenarios are plausible and are not mutually exclusive, and a feedback process is possible whereby fluids transporting radiogenic Sr imprint high $^{87}Sr/^{86}Sr$ ratios onto shear zone rocks and minerals, and subsequent fluid circulation partially scavenges such radiogenic Sr during circulation along the shear zones. Our discussion of Sr isotope data highlights the complexity of the patterns of fluid circulation in highly deformed granitoids well, in which fluid dynamics and chemistry are determined by but at the same time influence the chemistry of the deforming host rock. The complex geodynamic evolution of the Aar Massif and the involvement of Variscan, Mesozoic, and Cenozoic units in deformation and water release imply that fluid pathways are isotopically heterogeneous among different localities. Targeting the same type of mineral (i.e., minerals of the epidote–clinozoisite solid solution series here) for both geochronological and geochemical constraints has permitted a more-direct comparison of the information extracted by different isotope systems. However, complementary insight into fluid circulation in such complex contexts may be gained by combining such an approach with detailed petrographic, microstructural, and geochemical investigations of cogenetic mineral phases. This would help to understand the interplay between shear zones and fluid circulation in affecting the geochemical budget of deformed granitoids in orogens.

Appendix A: Tera–Wasserburg diagrams of allanite secondary reference materials

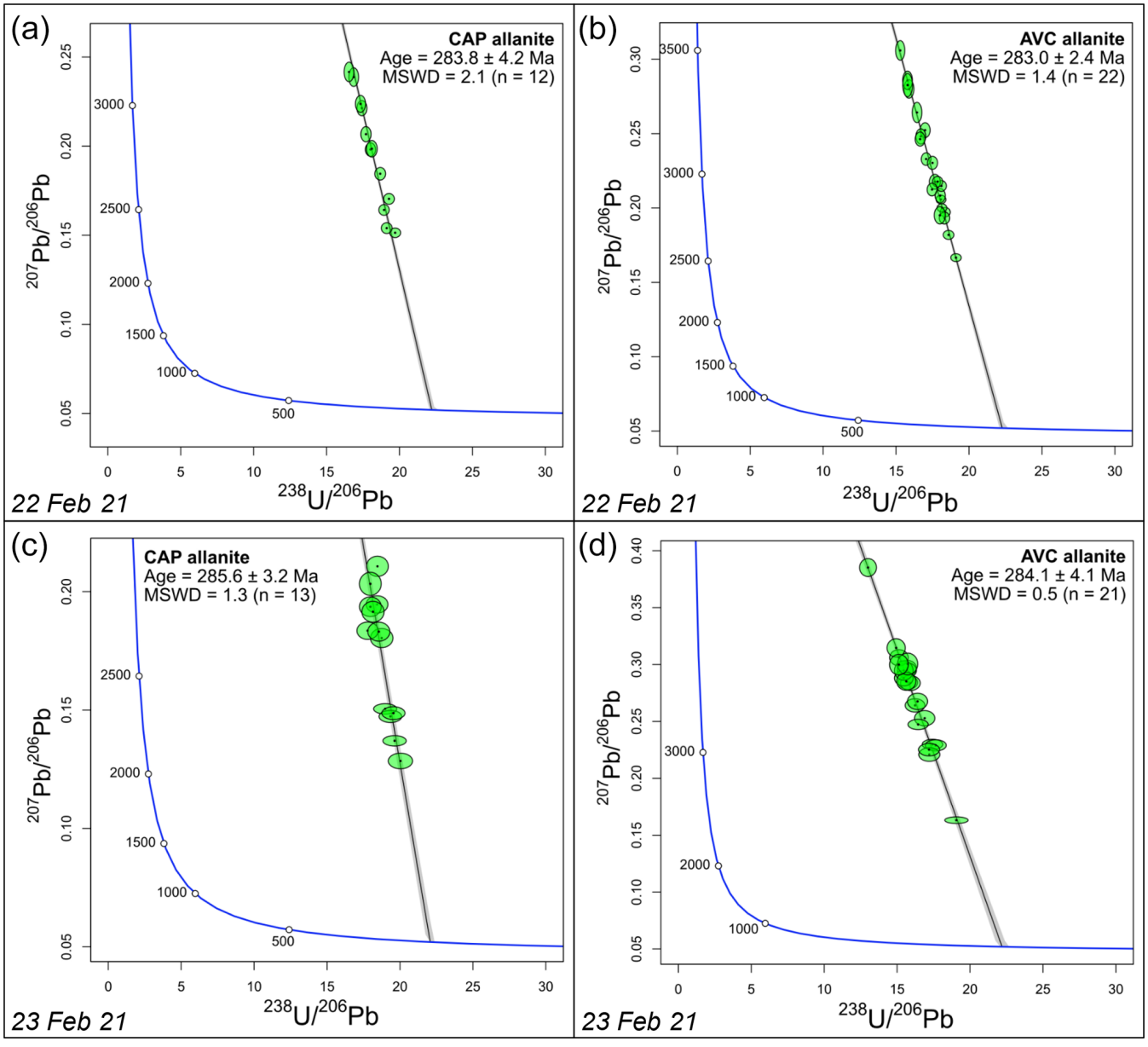

Figure A1. Tera–Wasserburg diagrams of allanite: **(a)** CAP (22 February 2021 session), **(b)** AVC (22 February 2021 session), **(c)** CAP (23 February 2021 session), and **(d)** AVC (23 February 2021 session) used as secondary reference materials for quality control for epidote U–Pb dating. The allanite reference materials are described in Barth et al. (1994) and Gregory et al. (2007). All regressions are anchored to a ^{207}Pb / ^{206}Pb value of 0.854 ± 0.015 (at 275 Ma; Stacey and Kramers, 1975). Plotted using IsoplotR (Vermeesch, 2018).

Appendix B: Location of samples P6b and P8 in the Grimsel test site

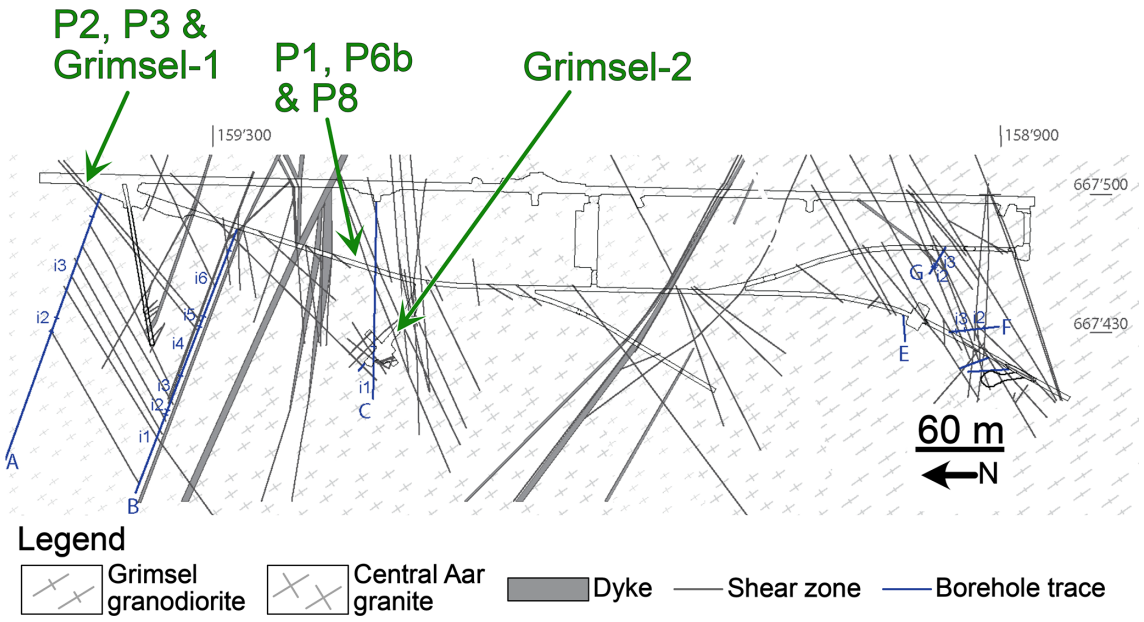

Figure B1. Location of Miocene samples P6b and P8 inside the Grimsel test site and in relation with previously published samples P1, P2, P3, Grimsel-1, and Grimsel-2. Modified from Schneeberger et al. (2019) and Peverelli et al. (2022a).

Data availability. All U–Pb isotope data are available in the Supplement (Tables S2–S3). Trace element (ΣREE, Pb, U, and Th) data are available in Table S4 in the Supplement. Sr–O–H isotope data are in Table 1 of this paper.

Sample availability. Samples can be obtained from the corresponding author upon request.

Supplement. The supplement related to this article is available online at: https://doi.org/10.5194/ejm-36-879-2024-supplement.

Author contributions. VP prepared all samples for measurements, carried out all analyses and laboratory work except for those related to H and O isotope measurements, and prepared the paper. AB and MH supervised the work, collected most samples, and provided insight into the structural aspect of this work. MW supervised the work in the clean laboratory and the measurements by TIMS and Neptune MC-ICP-MS. TP helped with data interpretation and granted access to the LA-ICP-MS laboratory. BP carried out O isotope measurements and helped with data interpretation. AM managed H isotope measurements and helped with data interpretation. EG provided sample Planggenstock and helped with interpretation of fluid circulation dynamics. All authors read the paper and contributed to its improvement.

Competing interests. The contact author has declared that none of the authors has any competing interests.

Disclaimer. Publisher's note: Copernicus Publications remains neutral with regard to jurisdictional claims made in the text, published maps, institutional affiliations, or any other geographical representation in this paper. While Copernicus Publications makes every effort to include appropriate place names, the final responsibility lies with the authors.

Acknowledgements. We thank Yann Rolland and an anonymous reviewer for their constructive feedback and Elisabetta Rampone and Qun-Ke Xia for handling the manuscript. The authors thank Daniela Rubatto for providing the allanite reference materials and Ferdinando Musso Piantelli for providing sample OBA19-03B. We acknowledge Nagra for granting access to the GTS. We thank Ulrich Treffert for H isotope measurements and Francesca Piccoli for technical assistance in the LA-ICP-MS laboratory. This work was carried out as part of project 178785 granted to Alfons Berger by the Swiss National Science Foundation. We acknowledge the funding of the new LA-ICP-MS facility through the Swiss National Science Foundation, project 206021_170722, to Daniela Rubatto and Thomas Pettke. The solution ICP-MS isotope data were obtained on a Neptune MC-ICP mass spectrometer acquired with funds from the NCCR PlanetS, supported by the Swiss National Science Foundation under grant no. 51NF40-141881.

Financial support. This research has been supported by the Schweizerischer Nationalfonds zur Förderung der Wissenschaftlichen Forschung (grant no. 178785).

Review statement. This paper was edited by Qun-Ke Xia and reviewed by Yann Rolland and one anonymous referee.

References

Abrecht, J. and Schaltegger, U.: Aplitic intrusions in the Central Aar massif basement: geology, petrography and Rb / Sr data, Eclogae Geol. Helv., 81, 227–239, 1988.

Barth, S., Oberli, F., and Meier, M.: ThPb versus UPb isotope systematics in allanite from co-genetic rhyolite and granodiorite: implications for geochronology, Earth Planet. Sc. Lett., 124, 149–159, https://doi.org/10.1016/0012-821X(94)00073-5, 1994.

Baumberger, R., Herwegh, M., and Kissling, E.: Remote sensing and field data based structural 3D modelling (Haslital, Switzerland) in combination with uncertainty estimation and verification by underground data, 3D Digital Geological Models: From Terrestrial Outcrops to Planetary Surfaces, 159–197, https://doi.org/10.1002/9781119313922.ch10, 2022.

Bergemann, C., Gnos, E., Berger, A., Whitehouse, M., Mullis, J., Wehrens, P., Pettke, T., and Janots, E.: Th-Pb ion probe dating of zoned hydrothermal monazite and its implications for repeated shear zone activity: An example from the central alps, Switzerland, Tectonics, 36, 671–689, https://doi.org/10.1002/2016TC004407, 2017.

Berger, A. and Herwegh, M.: Cockade structures as a paleoearthquake proxy in upper crustal hydrothermal systems, Sci. Rep., 9, 9209, https://doi.org/10.1038/s41598-019-45488-2, 2019.

Berger, A. and Herwegh, M.: Grain-size-reducing- and mass-gaining processes in different hydrothermal fault rocks, Geol. Mag., 159, 2219–2237, https://doi.org/10.1017/S0016756822000218, 2022.

Berger, A., Gnos, E., Janots, E., Whitehouse, M., Soom, M., Frei, R., and Waight, T. E.: Dating brittle tectonic movements with cleft monazite: Fluid-rock interaction and formation of REE minerals, Tectonics, 32, 1176–1189, https://doi.org/10.1002/tect.20071, 2013.

Berger, A., Wehrens, P., Lanari, P., Zwingmann, H., and Herwegh, M.: Microstructures, mineral chemistry and geochronology of white micas along a retrograde evolution: An example from the Aar massif (Central Alps, Switzerland), Tectonophysics, 721, 179–195, https://doi.org/10.1016/j.tecto.2017.09.019, 2017a.

Berger, A., Mercolli, I., Herwegh, M., and Gnos, E.: Geological Map of the Aar Massif, Tavetsch and Gotthard Nappes, Geol. spec. Map 1 V 100000, explanatory notes 129, Federal Office of Topogaphy swisstopo, Bern, Switzerland, ISBN: 978-3-302-40093-8, 2017b.

Berger, A., Egli, D., Glotzbach, C., Valla, P. G., Pettke, T., and Herwegh, M.: Apatite low-temperature chronometry and microstructures across a hydrothermally active fault zone, Chem. Geol., 588, 120633, https://doi.org/10.1016/j.chemgeo.2021.120633, 2022.

Bird, D. K. and Spieler, A. R.: Epidote in Geothermal Systems, Trace element geochemistry of epidote minerals, Rev. Mineral. Geochem., 56, 235–300, https://doi.org/10.2138/gsrmg.56.1.235, 2004.

Bodnar, R. J., Lecumberri-Sanchez, P., Moncada, D., and Steele-MacInnis, M.: Fluid Inclusions in Hydrothermal Ore Deposits, 2nd Edn., Elsevier Ltd., 119–142, https://doi.org/10.1016/B978-0-08-095975-7.01105-0, 2013.

Buehler, M., Zurbriggen, R., Berger, A., Herwegh, M., and Rubatto, D.: Late Carboniferous Schlingen in the Gotthard nappe (Central Alps) and their relation to the Variscan evolution, Int. J. Earth Sci., 112, 417–442, https://doi.org/10.1007/s00531-022-02247-5, 2023.

Cenki-Tok, B., Darling, J. R., Rolland, Y., Dhuime, B., and Storey, C. D.: Direct dating of mid-crustal shear zones with synkinematic allanite: New in situ U-Th-Pb geochronological approaches applied to the Mont Blanc massif, Terra Nov., 26, 29–37, https://doi.org/10.1111/ter.12066, 2014.

Chacko, T., Riciputi, R., Cole, R., and Horita, J.: A new technique for determining equilibrium hydrogen isotope fractionation factors using the ion microprobe: Application to the epidote-water system, Geochim. Cosmochim. Ac., 63, 1–10, https://doi.org/10.1016/S0016-7037(99)00007-1, 1999.

Challandes, N., Marquer, D., and Villa, I. M.: P-T-t modelling, fluid circulation, and 39Ar-40Ar and Rb-Sr mica ages in the Aar Massif shear zones (Swiss Alps), Swiss J. Geosci., 101, 269–288, https://doi.org/10.1007/s00015-008-1260-6, 2008.

Chew, D. M., Petrus, J. A., and Kamber, B. S.: U-Pb LA-ICPMS dating using accessory mineral standards with variable common Pb, Chem. Geol., 363, 185–199, https://doi.org/10.1016/j.chemgeo.2013.11.006, 2014.

Dempster, T. J.: Isotope systematics in minerals: biotite rejuvenation and exchange during Alpine metamorphism, Earth Planet. Sc. Lett., 78, 355–367, https://doi.org/10.1016/0012-821X(86)90003-8, 1986.

Diamond, L. W., Wanner, C., and Waber, H. N.: Penetration depth of meteoric water in orogenic geothermal systems, Geology, 46, 1–4, https://doi.org/10.1130/G45394.1, 2018.

Franz, G. and Liebscher, A.: Physical and Chemical Properties of the Epidote Minerals – An Introduction, Rev. Mineral. Geochem., 56, 1–81, https://doi.org/10.2138/gsrmg.56.1.1, 2004.

Frei, D., Liebscher, A., Franz, G., and Dulski, P.: Trace element geochemistry of epidote minerals, Rev. Mineral. Geochem., 56, 553–605, https://doi.org/10.2138/gsrmg.56.1.553, 2004.

Fricke, H. C., Wickham, S. M., and O'Neil, J. R. O.: Oxygen and hydrogen isotope evidence for meteoric water infiltration during mylonitization and uplift in the Ruby Mountains-East Humboldt Range core complex, Nevada, Contrib. Mineral. Petrol., 111, 203–221, https://doi.org/10.1007/BF00348952, 1992.

Gnos, E., Mullis, J., Ricchi, E., Bergemann, C. A., Janots, E., and Berger, A.: Episodes of fissure formation in the Alps: connecting quartz fluid inclusion, fissure monazite age, and fissure orientation data, Swiss J. Geosci., 114, 14, https://doi.org/10.1186/s00015-021-00391-9, 2021.

Goncalves, P., Oliot, E., Marquer, D., and Connolly, J. A. D.: Role of chemical processes on shear zone formation: An example from the grimsel metagranodiorite (Aar massif, Central Alps), J.

Metamorph. Geol., 30, 703–722, https://doi.org/10.1111/j.1525-1314.2012.00991.x, 2012.

Grambling, T. A., Jessup, M. J., Newell, D. L., Methner, K., Mulch, A., Hughes, C. A., and Shaw, C. A.: Miocene to modern hydrothermal circulation and high topography during synconvergent extension in the Cordillera Blanca, Peru, Geology, 50, 106–110, https://doi.org/10.1130/G49263.1, 2022.

Gregory, C. J., Rubatto, D., Allen, C. M., Williams, I. S., Hermann, J., and Ireland, T.: Allanite micro-geochronology: A LA-ICP-MS and SHRIMP U-Th-Pb study, Chem. Geol., 245, 162–182, https://doi.org/10.1016/j.chemgeo.2007.07.029, 2007.

Herwegh, M., Berger, A., Baumberger, R., Wehrens, P., and Kissling, E.: Large-Scale Crustal-Block-Extrusion During Late Alpine Collision, Sci. Rep., 7, 1–10, https://doi.org/10.1038/s41598-017-00440-0, 2017.

Herwegh, M., Berger, A., Glotzbach, C., Wangenheim, C., Mock, S., Wehrens, P., Baumberger, R., Egli, D., and Kissling, E.: Late stages of continent-continent collision: Timing, kinematic evolution, and exhumation of the Northern rim (Aar Massif) of the Alps, Earth-Sci. Rev., 200, 102959, https://doi.org/10.1016/j.earscirev.2019.102959, 2020.

Herwegh, M., Berger, A., Bellahsen, N., Rolland, Y., and Kissling, E.: Evolution of the external crystalline massifs of the European Alps: From massif to lithosphere scale, Geodynamics of the Alps 3 Collisional Processes, 53–99, https://doi.org/10.1002/9781394299560.ch2, 2022.

Hofmann, B. A., Helfer, M., Diamond, L. W., Villa, I. M., Frei, R., and Eikenberg, J.: Topography-driven hydrothermal breccia mineralization of Pliocene age at Grimsel Pass, Aar massif, Central Swiss Alps, Schweiz. Miner. Petrog., 84, 271–302, 2004.

Horwitz, E., Dietz, M. L., and Chiarizia, R.: The application of novel extraction chromatographic materials to the characterization of radioactive waste solutions, J. Radioanal. Nucl. Chem., 161, 575–583, 1992.

Janots, E., Berger, A., Gnos, E., Whitehouse, M., Lewin, E., and Pettke, T.: Constraints on fluid evolution during metamorphism from U-Th-Pb systematics in Alpine hydrothermal monazite, Chem. Geol., 326/327, 61–71, https://doi.org/10.1016/j.chemgeo.2012.07.014, 2012.

Keusen, H.R., Ganguin, J., Schuler, P., and Buletti, M.: Grimsel test site: geology (NAGRA-NTB–87-14), Switzerland, 1989.

Lacroix, B. and Vennemann, T.: Empirical calibration of the oxygen isotope fractionation between quartz and Fe-Mg-chlorite, Geochim. Cosmochim. Ac., 149, 21–31, https://doi.org/10.1016/j.gca.2014.10.031, 2015.

Malatesta, C., Crispini, L., Ildefonse, B., Federico, L., Lisker, F., and Läufer, A.: Microstructures of epidote-prehnite bearing damaged granitoids (northern Victoria Land, Antarctica): clues for the interaction between faulting and hydrothermal fluids, J. Struct. Geol., 147, 104350, https://doi.org/10.1016/j.jsg.2021.104350, 2021.

Marquer, D. and Burkhard, M.: Fluid circulation, progressive deformation and mass-transfer processes in the upper crust: the example of basement-cover relationships in the External Crystalline Massifs, Switzerland, J. Struct. Geol., 14, 1047–1057, https://doi.org/10.1016/0191-8141(92)90035-U, 1992.

Marquer, D. and Peucat, J. J.: Rb-Sr systematics of recrystallized shear zones at the greenschist- amphibolite transition: examples from granites in the Swiss central Alps, Schweiz. Miner. Petrog., 74, 343–358, 1994.

McArthur, J. M., Howarth, R. J., and Shields, G. A.: Strontium isotope stratigraphy, Geol. Time Scale 2012, 127–144, https://doi.org/10.1016/B978-0-444-59425-9.00007-X, 2012.

Menzies, C. D., Teagle, D. A. H., Craw, D., Cox, S. C., Boyce, A. J., Barrie, C. D., and Roberts, S.: Incursion of meteoric waters into the ductile regime in an active orogen, Earth Planet. Sc. Lett., 399, 1–13, https://doi.org/10.1016/j.epsl.2014.04.046, 2014.

Mulch, A. and Chamberlain, C. P.: Stable Isotope Paleoaltimetry in Orogenic Belts – The silicate record in surface and crustal geological archives, Rev. Mineral. Geochem., 66, 89–118, https://doi.org/10.2138/rmg.2007.66.4, 2007.

Mulch, A., Teyssier, C., Cosca, M. A., Vanderhaeghe, O., and Vennemann, T. W.: Reconstructing paleoelevation in eroded orogens, Geology, 32, 525–528, https://doi.org/10.1130/G20394.1, 2004.

Musso Piantelli, F., Mair, D., Berger, A., Schlunegger, F., Wiederkehr, M., Kurmann, E., Baumberger, R., Möri, A., and Herwegh, M.: 4D reconstruction of the Doldenhorn nappe-basement system in the Aar massif: Insights into late-stage continent-continent collision in the Swiss Alps, Tectonophysics, 843, 229586, https://doi.org/10.1016/j.tecto.2022.229586, 2022.

Oberhänsli, R., Schenker, F., and Mercolli, I.: Indications of Variscan nappe tectonics in the Aar Massif, Schweiz. Mineral. Petrog., 68, 509–520, 1988.

Oliot, E., Goncalves, P., and Marquer, D.: Role of plagioclase and reaction softening in a metagranite shear zone at mid-crustal conditions (Gotthard Massif, Swiss Central Alps), J. Metamorph. Geol., 28, 849–871, https://doi.org/10.1111/j.1525-1314.2010.00897.x, 2010.

Peverelli, V., Ewing, T., Rubatto, D., Wille, M., Berger, A., Villa, I. M., Lanari, P., Pettke, T., and Herwegh, M.: U–Pb geochronology of epidote by laser ablation inductively coupled plasma mass spectrometry (LA-ICP-MS) as a tool for dating hydrothermal-vein formation, Geochronology, 3, 123–147, https://doi.org/10.5194/gchron-3-123-2021, 2021.

Peverelli, V., Berger, A., Mulch, A., Pettke, T., Piccoli, F., and Herwegh, M.: Epidote U-Pb geochronology and H isotope geochemistry trace pre-orogenic hydration of midcrustal granitoids, Geology, 50, 1073–1077, https://doi.org/10.1130/G50028.1, 2022a.

Peverelli, V., Berger, A., Wille, M., Pettke, T., Lanari, P., Villa, I. M., and Herwegh, M.: Epidote dissolution – precipitation during viscous granular flow: a micro-chemical and isotope study, Solid Earth, 13, 1803–1821, https://doi.org/10.5194/se-13-1803-2022, 2022.

Peverelli, V., Berger, A., Wille, M., Mulch, A., Lanari, P., Pettke, T., Putlitz, B., and Herwegh, M.: Unravelling the hydration history of an inverted passive continental margin using epidote U[sbnd]Pb geochronology and Pb–Sr–O–H isotope geochemistry, Lithos, 460–461, 107391, https://doi.org/10.1016/j.lithos.2023.107391, 2023.

Pfiffner, O. A.: The structure of the Helvetic nappes and its relation to the mechanical stratigraphy. Journal of Structural Geology, 15, 511–521, https://doi.org/10.1016/0191-8141(93)90145-Z, 1993.

Ricchi, E., Bergemann, C. A., Gnos, E., Berger, A., Rubatto, D., and Whitehouse, M. J.: Constraining deformation phases in the Aar Massif and the Gotthard Nappe (Switzerland) using Th-Pb crystallization ages of fissure monazite-(Ce), Lithos, 342/343, 223–238, https://doi.org/10.1016/j.lithos.2019.04.014, 2019.

Rolland, Y., Cox, S. F., and Corsini, M.: Constraining deformation stages in brittle-ductile shear zones from combined field mapping and $^{40}Ar/^{39}Ar$ dating: The structural evolution of the Grimsel Pass area (Aar Massif, Swiss Alps), J. Struct. Geol., 31, 1377–1394, https://doi.org/10.1016/j.jsg.2009.08.003, 2009.

Rossi, M. and Rolland, Y.: Stable isotope and Ar/Ar evidence of prolonged multiscale fluid flow during exhumation of orogenic crust: Example from the mont blanc and Aar Massifs (NW Alps), Tectonics, 33, 1681–1709, https://doi.org/10.1002/2013TC003438, 2014.

Ruiz, M., Schaltegger, U., Gaynor, S. P., et al.: Reassessing the intrusive tempo and magma genesis of the late Variscan Aar batholith: U–Pb geochronology, trace element and initial Hf isotope composition of zircon, Swiss J. Geosci., 115, 20, https://doi.org/10.1186/s00015-022-00420-1, 2022.

Sheppard, S. M. F.: Characterization and isotopic variations in natural waters, Stable Isotopes in High Temperature Geological Processes, 165–183, https://doi.org/10.1515/9781501508936-011, 2019.

Schaltegger, U.: The Central Aar Granite: Highly differentiated calc-alkaline magmatism in the Aar Massif (Central Alps, Switzerland), Eur. J. Mineral., 2, 245–260, https://doi.org/10.1127/ejm/2/2/0245, 1990.

Schaltegger, U.: The evolution of the polymetamorphic basement in the Central Alps unravelled by precise U-Pb zircon dating, Contrib. Mineral. Petrol., 113, 466–478, https://doi.org/10.1007/BF00698316, 1993.

Schaltegger, U. and Corfu, F.: The age and source of late Hercynian magmatism in the central Alps: evidence from precise U-Pb ages and initial Hf isotopes, Contrib. Mineral. Petrol., 111, 329–344, https://doi.org/10.1007/BF00311195, 1992.

Schlunegger, F., Leu, W., and Matter, A.: Sedimentary sequences, seismic facies, subsidence analysis, and evolution of the Burdigalian Upper Marine Molasse Group, central Switzerland, Am. Assoc. Pet. Geol. Bull., 81, 1185–1207, https://doi.org/10.1306/522b4a19-1727-11d7-8645000102c1865d, 1997.

Schneeberger, R., Kober, F., Lanyon, G. W., Mäder, U. K., Spillmann, T., and Blechschmidt, I.: Grimsel Test Site: Revisiting the site-specific geoscientific knowledge, 2019.

Schwartz, S., Rolland, Y., Nouibat, A., Boschetti, L., Bienveignant, D., Dumont, T., Mathey, M., Sue, C., and Mouthereau, F.: Role of mantle indentation in collisional deformation evidenced by deep geophysical imaging of Western Alps, Commun. Earth Environ., 5, 1–9, https://doi.org/10.1038/s43247-023-01180-y, 2024.

Smye, A. J., Roberts, N. M. W., Condon, D. J., Horstwood, M. S. A., and Parrish, R. R.: Characterising the U-Th-Pb systematics of allanite by ID and LA-ICPMS: Implications for geochronology, Geochim. Cosmochim. Ac., 135, 1–28, https://doi.org/10.1016/j.gca.2014.03.021, 2014.

Steck, A.: Die alpidischen Strukturen in den zentralen Aaregraniten des westlichen Aarmassivs, Eclogae Geol. Helv., 61, 19–48, 1968.

Stipp, M., Stünitz, H., Heilbronner, R., and Schmid, S. M.: Dynamic recrystallization of quartz: correlation between natural and experimental conditions, Geol. Soc. Lond. Sp. Publ., 200, 171–190, https://doi.org/10.1144/GSL.SP.2001.200.01.11, 2002.

Taylor, H. P.: Water/rock interactions and the origin of H2O in granitic batholiths, J. Geol. Soc. Lond., 133, 509–558, https://doi.org/10.1144/gsjgs.133.6.0509, 1977.

Taylor, H. P.: Oxygen and hydrogen isotope studies of plutonic granitic rocks, Dev. Petrol., 5, 177–210, 1978.

Vermeesch, P.: IsoplotR: A free and open toolbox for geochronology, Geosci. Front., 9, 1479–1493, https://doi.org/10.1016/j.gsf.2018.04.001, 2018.

Wehrens, P., Berger, A., Peters, M., Spillmann, T., and Herwegh, M.: Deformation at the frictional-viscous transition: Evidence for cycles of fluid-assisted embrittlement and ductile deformation in the granitoid crust, Tectonophysics, 693, 66–84, https://doi.org/10.1016/j.tecto.2016.10.022, 2016.

Wehrens, P., Baumberger, R., Berger, A., and Herwegh, M.: How is strain localized in a meta-granitoid, mid-crustal basement section? Spatial distribution of deformation in the central Aar massif (Switzerland), J. Struct. Geol., 94, 47–67, https://doi.org/10.1016/j.jsg.2016.11.004, 2017.

Weis, D., Kieffer, B., Maerschalk, C., Barling, J., De Jong, J., Williams, G. A., Hanano, D., Pretorius, W., Mattielli, N., Scoates, J. S., Goolaerts, A., Friedman, R. M., and Mahoney, J. B.: High-precision isotopic characterization of USGS reference materials by TIMS and MC-ICP-MS, Geochem. Geophy. Geosy., 7, Q08006, https://doi.org/10.1029/2006GC001283, 2006.

Wintsch, R. P., Christoffersen, R., and Kronenberg, A. K.: Fluid-rock reaction weakening of fault zones, J. Geophys. Res., 100, 13021–13032, https://doi.org/10.1029/94jb02622, 1995.

Yardley, B. W. D: 100th Anniversary Special Paper: Metal Concentrations in Crustal Fluids and Their Relationship to Ore Formation, Econ. Geol., 100, 613–632, https://doi.org/10.2113/gsecongeo.100.4.613, 2005.

Yardley, B. W. D. and Cleverley, J. S.: The role of metamorphic fluids in the formation of ore deposits, Geol. Soc. Spec. Publ., 393, 117–134, https://doi.org/10.1144/SP393.5, 2014.

Yardley, B. W. D. and James, S. C.: The role of metamorphic fluids in the formation of ore deposits, London, The Geological Society of London, https://doi.org/10.1144/sp393.5, 2015.

Zhan, W., Nevskaya, N., Niemeijer, A., Berger, A., Spiers, C., and Herwegh, M.: Hydrothermal Alteration-Induced Weakening in Experimentally Deformed Fault Gouges, EGU General Assembly 2024, Vienna, Austria, 14–19 Apr 2024, EGU24-17448, https://doi.org/10.5194/egusphere-egu24-17448, 2024.

Zheng, Y. F.: Calculation of oxygen isotope fractionation in hydroxyl-bearing silicates, Earth Planet. Sc. Lett., 121, 247–263, https://doi.org/10.1016/0012-821X(93)90243-3, 1993.